Research Square

Preprints are preliminary reports that have not undergone peer review.
They should not be considered conclusive, used to inform clinical practice,
or referenced by the media as validated information.

ZnAl LDH/MnAl2O3 biphasic material as an efficient adsorbent and catalyst for the reduction of hexavalent chromium in aqueous solution

Guadalupe Romero Ortiz

tomitzi_21@hotmail.com

UAM Iztapalapa: Universidad Autonoma Metropolitana - Iztapalapa https://orcid.org/0000-0001-7189-1742

Francisco Tzompantzi

UAM: Universidad Autonoma Metropolitana

Luis Lartundo Rojas

IPN: Instituto Politecnico Nacional

Angeles Mantilla

Instituto Politecnico Nacional https://orcid.org/0000-0002-3273-3095

Research Article

Keywords: Galaxite, biphasic material, hydrotalcite (LDH), manganese, Cr (VI)

Posted Date: June 15th, 2026

DOI: https://doi.org/10.21203/rs.3.rs-9784697/v1

License: This work is licensed under a Creative Commons Attribution 4.0 International License.
Read Full License

ZnAl LDH/$MnAl_2O_3$ biphasic material as an efficient adsorbent and catalyst for the reduction of hexavalent chromium in aqueous solution.

Guadalupe Romero-Ortiz[1,2], Francisco Tzompantzi[1], Luis Lartundo-Rojas[3] and Angeles Mantilla[2]*

[1]Universidad Autónoma Metropolitana - Iztapalapa. Av. San Rafael Atlixco No. 186, Leyes de Reforma, 09340, Ciudad de México, México.

[2]Instituto Politécnico Nacional, Laboratorio de Fotocatálisis, CICATA-Legaria, Legaria 694, Col. Irrigación, 11500, Ciudad de México, México.

[3]Instituto Politécnico Nacional, Centro de Nanociencias y Micro y Nanotecnologías, Luis Enrique Erro s/n, Zacatenco, 07320, Ciudad de México, México.

*Corresponding author: mmantillar@ipn.mx.

Keywords: Galaxite, biphasic material, hydrotalcite (LDH), manganese, Cr (VI).

Abstract

Hexavalent chromium (Cr(VI)) is one of the most hazardous inorganic contaminants in aquatic environments due to its high toxicity and mobility. In this work, ZnAl layered double hydroxides (ZnAl-LDH) and a biphasic composite consisting of ZnAl hydrotalcite and MnAl mixed oxide (ZnMnAl) were synthesized by the coprecipitation method at room temperature and evaluated for Cr (VI) removal from aqueous solutions. Adsorption experiments were conducted at initial Cr (VI) concentrations ranging from 40 to 200 ppm, assessing the influence of adsorbent dosage, solution pH, point of zero charge (pH_{pzc}), contact time, and adsorbent physical form (powder and pill). The ZnMnAl composite exhibited a significantly higher adsorption performance than ZnAl-LDH, achieving a maximum removal efficiency of up to 97% and a maximum adsorption capacity of 200 mg·g−1, as determined from Langmuir isotherm modeling. Kinetic studies revealed that Cr(VI) adsorption followed a pseudo-first-order model under immediate analysis conditions, while aged samples (24 h resting time) were better described by a pseudo-second-order model, indicating a time-dependent adsorption mechanism. The powder form of ZnMnAl showed superior performance compared to the pelletized material, which exhibited lower removal efficiencies over repeated adsorption cycles. Structural, textural, and surface properties of the materials were characterized using XRD, BET, FTIR, SEM, UV–Vis, and XPS techniques. These results demonstrate that the biphasic ZnMnAl material is a promising adsorbent for the efficient removal of Cr(VI) from contaminated water.

1. Introduction

Over the years, several inorganic contaminants (heavy metals) present in water have caused adverse damage to habitats and the health of living organisms(Ahmed and Mohamed 2023), leading to growing interest in the development of new and improved materials with high capacities for the removal of inorganic contaminants from water. Heavy metals originating from electroplating,

mining, metallurgy, and battery manufacturing—which nowadays are intensively used in the development of new technologies such as electric vehicles—continuously release lead (Pb), cadmium (Cd), and chromium (Cr) into different water bodies. This release generates adverse effects on ecosystems and human health and remains a topic of significant concern, as water scarcity, limited access, and the low efficiency of conventional treatment processes hinder the achievement of water supplies with adequate quality and safety standards(Shen et al. 2025).

In recent years, Cr(VI) contamination has increased throughout Latin America. Cr(VI) is considered a stable, mobile, and highly toxic contaminant that damages plant and animal tissues and is classified as a Group 1 mutagenic and carcinogenic agent by the World Health Organization. The United States Environmental Protection Agency (USEPA) has identified Cr(VI) as a contaminant of major concern due to its high solubility, enhanced toxicity, and carcinogenic nature compared to Cr(III). The maximum permissible levels of Cr(VI) are 50 $\mu g \cdot L^{-1}$ in drinking water and 200 $\mu g \cdot L^{-1}$ in industrial effluents(Zhang et al. 2025). Furthermore, Cr(VI) can easily disperse through untreated wastewater streams that reach aquifers, rivers, lakes, and seas, subsequently contaminating soils, flora, and fauna. Once released into the environment, chromium is not biologically degradable and can persist for hundreds of years, making rapid and efficient remediation difficult. As a result, many living organisms have been affected due to its tendency to accumulate in plants, soils, and organic tissues, with the highest concentrations commonly found in the kidneys, liver, and bones(Hashem et al. 2025; Sivaranjanee et al. 2022).

Chromium exists in several oxidation states, including Cr(II) (+2), Cr(III) (+3), and Cr(IV) (+4). The hexavalent state Cr(VI), is the second most stable oxidation state and the most toxicologically relevant. Therefore, the development of methods and materials capable of removing Cr(VI) or reducing it to the more stable and less toxic trivalent state of chromium (Cr(III) form) is of great importance. Cr(III) is an essential trace element in living organisms, playing a role in the metabolism of fatty acids, glucose, cholesterol, and various biological processes. Cr(VI) is particularly difficult to degrade due to its tendency to accumulate in living organisms and, in aqueous solution, it exists primarily as oxyanions such as chromate (CrO_4^{2-}), hydrogen chromate ($HCrO_4^-$), and dichromate ($Cr_2O_7^{2-}$), all of which are highly toxic and responsible for severe adverse effects in humans and other living beings(Ogata et al. 2018).

It is therefore necessary to improve and optimize water treatment processes and materials in order to achieve higher removal efficiency while ensuring that the processes are environmentally friendly, reusable, and cost-effective. Currently, various treatment strategies aim to remove heavy metals using adsorbent materials based on layered double hydroxides (LDHs), including isomorphic substitution, surface adsorption, anion coordination within the interlayer space, interlayer redox reactions, and ion exchange processes(He et al. 2023). Among these approaches, adsorption has been widely recognized as an effective physicochemical process for the removal of heavy metal ions. Within the range of available adsorbents, hydrotalcites, both untreated and thermally treated, have demonstrated efficient removal of Cr(VI) from aqueous solutions. For instance, calcined magnesium–aluminum hydrotalcites have been used as adsorbents and intercalating agents for Cr(VI) removal, while calcium–aluminum hydrotalcites have been employed for the adsorption of chromium(VI) nitrate(Li et al. 2013) and uranium(VI), exhibiting high adsorption capacities.

Layered double hydroxides (LDHs), also known as hydrotalcites, are environmentally friendly clay-like materials widely applied in environmental remediation due to their favorable properties as adsorbents, including high anion exchange capacity, tunable structure through divalent and trivalent metal substitution, and high specific surface area (Ahmed c Mohamed 2023; Feng et al. 2022; He et al. 2023; Zhang et al. 2022).

LDHs are derived from the brucite structure ($Mg(OH)_2$), in which hydroxyl groups are octahedrally coordinated to Mg^{2+} ions. The sharing of octahedral edges leads to the formation of layered structures. Partial substitution of Mg^{2+} by other metal cations results in positively charged layers, which are electrically balanced by the incorporation of anions between adjacent layers, forming a sandwich-like structure.

LDHs have the general formula $[M^{2+}_{1-x}M^{3+}_{x}(OH)_2]^{x+}(A^{n-})_{x/n}\cdot mH_2O$, where M^{2+} represents a divalent cation (e.g., Mg, Co, Cu, Ni, and Zn), M^{3+} represents a trivalent cation, and the type and proportion of metal cations strongly influence the structure and chemical properties of the material(Solangi et al. 2026). A^{n-} represents charge-compensating anions, which may be inorganic or organic (e.g., Cl^-, NO_3^-, CO_3^{2-}, OH^-, SO_4^{2-}, PO_4^{3-}, $C_6H_4(COO)_2^{2-}$, and complex ions (Cao et al. 2024) The parameter x corresponds to the molar ratio of trivalent cations and typically ranges between 0.20 and 0.33 (Gherca et al. 2023; Zhou et al. 2024).

Hydrotalcites have been employed in a wide range of applications, including catalysis, nuclear waste immobilization, electroactive and photoactive materials, pharmaceutical products, anion scavengers, neutralizing agents (antacids), filters, polymer stabilizers, photocatalytic supports, and anion exchangers. Due to their unique physicochemical properties, LDHs are widely used as adsorbents, catalytic adsorbents, reducing adsorbents, and photocatalytic materials for the removal of various contaminants from water systems(Grainca et al. 2024; Li et al. 2013).

The affinity of hydrotalcites for these metallic ions is influenced by anion size, charge density, and temperature (Ogata et al. 2018), as well as by the intrinsic properties of the target heavy metal ions. Several mechanisms contribute to their removal, including physical adsorption, electrostatic attraction, ion exchange, anion–metal surface complexation (Zhou et al. 2024), and chemical bonding. In addition, various physicochemical processes such as precipitation, adsorption isotherms, adsorption kinetics, contact angle effects, capillary coagulation, acidity and alkalinity, isomorphic substitution, and chemical reduction play important roles in the remediation of water bodies contaminated with heavy metals (Gherca et al. 2023).

Hydrotalcites are environmentally friendly materials that are suitable for a wide range of reactions and offer significant advantages, including tunable properties and controllable structures, enabling the development of highly efficient materials for various environmental applications, particularly heavy metal removal. Accordingly, the main objective of this work was to remediate Cr(VI)-contaminated water using a biphasic composite material composed of ZnAl hydrotalcite and MnAl oxide (MnAlO), the latter of which has been reported as an effective adsorbent for recalcitrant contaminants (Picos-Benítez et al. 2024), This performance is attributed to the presence of manganese ions, which play a crucial role in the treatment of various pollutants(Dey and Praveen Kumar 2020; Wang et al. 2025; Yang et al. 2016).

Manganese exhibits multiple oxidation states, including Mn^{2+}, Mn^{3+}, Mn^{4+}, Mn^{5+}, Mn^{6+}, and Mn^{7+}, with Mn^{2+}, Mn^{3+}, and Mn^{4+} being the most common. These multiple oxidation states favor the interconversion of reactions involved in catalytic processes (Sun et al. 2023; Wang et al. 2025), such as reduction of different metallic ions (Wu et al. 2021) and electron transfer reactions, thereby enhancing surface redox activity(Miranda et al. 2022). Through a series of Cr(VI) adsorption experiments, the influence of contact time in a reactor at room temperature was experimentally evaluated. Comparative systems consisting of ZnAl-LDH and the biphasic ZnMnAl material were employed under different experimental conditions, considering key parameters affecting adsorption performance, including solution pH, initial Cr(VI) concentration, and catalyst dosage.

2. Materials and methods

2.1. Chemical

The salts used in the synthesis of the materials were reagent grade. $Zn(NO_3)_2{\cdot}6H_2O$ (≥98%, Sigma–Aldrich) and $Al(NO_3)_3{\cdot}9H_2O$ (98%, Sigma–Aldrich) were used as divalent metal (M^{2+}) and trivalent metal (M^{3+}) precursor, respectively; $MnCl_2{*}4H_2O$ (≥98%, MEYER Company) as modifying agent, CH_4N_2O (99%, MEYER Company) as a reducing agent, and NaOH (≥98%, Sigma–Aldrich) was used to adjust the pH of the solution.

2.2. Synthesis of ZnAl LDH and ZnMnAl biphasic material

ZnAl-LDH precursor material was synthesized using the coprecipitation method with a molar ratio of Zinc and Aluminum M^{2+}/M^{3+} of 3:1, respectively. In a three-necked glass round bottom flask, a saline solution was mixed in 100 mL of deionized water along with the corresponding amounts of Zinc nitrate ($Zn(NO_3)_2{\cdot}6H_2O$), aluminum nitrate ($Al(NO_3)_3{\cdot}9H_2O$) and urea (CH_4N_2O) as precipitating agent; additionally, a solution of NaOH at 0.4 molar was added drop by drop until a pH of 9 was obtained, the solution was kept stirring and at a constant temperature of 90°C and room temperature, it was allowed to age for 24 hours to obtain a precipitate, which was washed with deionized water to eliminate unwanted products, dried and crushed.

For the synthesis of ZnMnAl biphasic material, in addition to the salts and reagents mentioned for the synthesis of ZnAl-LDH, $MnCl_2{*}_4H_2O$ was additionally added as a modifying material to obtain a 2/1/1 ratio of Zn, Mn and Al, respectively.

2.3. Preparation of Cr solution.

To evaluate the adsorption tests, synthetic solutions of potassium dichromate ($K_2Cr_2O_7$, ≥99.0%, Sigma-Aldrich) were prepared at concentrations of 40 and 100 ppm. In addition, 0.025 g of citric acid ($C_6H_8O_7$, ≥99.5%, MEYER Company) and 50 µL of phosphoric acid (H_3PO_4, ≥85.0%, MEYER Company) were added to each 50 mL of potassium dichromate solution, resulting in a final pH of 2.

2.4. Characterization of biphasic material

Different characterization techniques were used to determine the properties of the materials. The surface morphology of the LDHs was evaluated by X-ray diffraction (XRD) using a Bruker AXS model D8 Advance diffractometer, equipped with an X-ray tube with a copper anode (λ = 1.5406 Å). Patterns were recorded in a 2θ range between 5° and 80°, with a scan rate of 2° min^{-1} and using a monochromator to select the Kα radiation. Fourier transform infrared spectroscopy (FTIR) was

performed on a Shimadzu IR Tracer-100 instrument, in a spectral range of 4000 to 500 cm^{-1}. Specific surface area was determined using the Brunauer–Emmett–Teller (BET) method, based on N_2 adsorption-desorption isotherms, with a surface area analyzer. The average pore diameter and volume were calculated using the Barrett–Joyner–Halenda (BJH) method, utilizing the desorption branch of the isotherm. Before analysis, the samples were degassed at 250 °C for 48 h.

X-ray photoelectron spectroscopy (XPS) of the LDH and the adsorbed compound was performed on a Thermo Scientific K-Al spectrometer, equipped with a monochromatic Al Kα source (1486.6 eV), to determine the elemental composition and chemical state of the elements on the material's surface.

The total Cr concentration in each aliquot of the solution was determined using the colorimetric method with diphenylcarbazide as the complexing agent. The concentrations of Cr (VI) after filtration were measured in a UV-Vis spectrophotometer at 540 nm. Likewise, the absorbance of the dichromate was monitored at 339 nm in a UV-Vis spectrophotometer, recording the spectral region between 300 and 800 nm.

2.5. Calibration curve (concentration)

To generate the calibration curve, 50 mL of a 100-ppm potassium dichromate solution was prepared, and from this solution, dilutions were made to obtain concentrations of 80, 60, 40, and 20 ppm. To each solution, 0.025 g of citric acid and 50 mL of phosphoric acid were added. UV–Vis spectroscopy was performed such in Figure 1a) using a Cary 100 spectrophotometer, monitoring the characteristic absorbance band of this compound at 338-339 nm. Figure 1b shows the regression line with a correlation coefficient of 0.9999, indicating satisfactory linearity, which was used to determine the concentrations after the adsorption process.

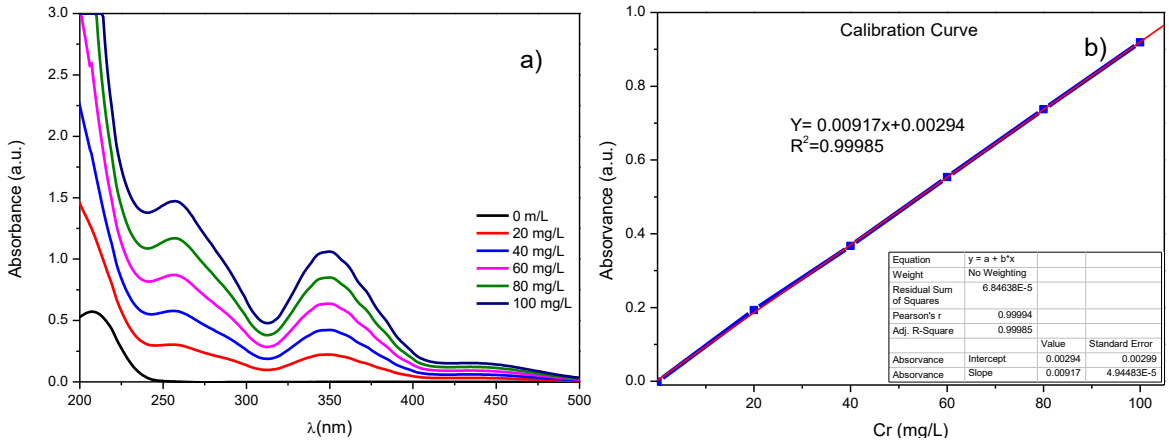


Figure 1 Maximum absorbance of potassium dichromate molecule ($K_2Cr_2O_7$) at 336nm of concentration ranges of 100, 80, 60, 40, 20 y 0ppm and b) linear regression fit of the different concentrations.

2.6. Calibration curve (colorimetric test)

Through the absorbance calibration curve, it is possible to reach the value of the final metal concentration (hexavalent chromium) of each of the aliquots taken during the adsorption process. To achieve this result, it is necessary to prepare the standard solutions using the colorimetric method. With this objective, the standard solutions prepared are analyzed through the

characterization technique by absorption spectrophotometry. From the absorbance data obtained from the standard solutions, the calibration line is obtained, and an adjustment is made by linear regression (See Graph 1).

Reagents:

I. Acetone (C_3H_6O)
II. Nitric acid (HNO_3) in water 1:1.
III. Concentrated sulfuric acid (H_2SO_4).
IV. Sulfuric acid 3 mol/L
V. Sulfuric acid 0,1 mol/L.
VI. Concentrated phosphoric acid (H_3PO_4).
VII. Sodium hidroxide (NaOH).
VIII. Ammonium sulphate $(NH_4)_2SO_4$.
IX. Ammonium hydroxide NH_40H.
X. Sodium hydroxide 5 mol/L.
XI. Sodium hydroxide 1 mol/L.
XII. Buffer dissolution: Dissolve 33 g of ammonium sulfate in 75 mL of water y add 6,5 mL of Ammonium hydroxide, bring to capacity 100 mL with water.
XIII. Potassium dichromate ($K_2Cr_2O_7$).
XIV. 1,5 Difenilcarbazida ($C_{13}H_{14}N_4O$).
XV. Diphenylcarbazide solution: Weigh 250 mg of 1,5-diphenylcarbazide and dissolve in 50 mL of acetone. Store in amber jars; This solution is transparent at the time of preparation, then it takes on a light-yellow color. Discard the solution when it begins to discolor; it should be kept refrigerated.
XVI. Stock reference solution of hexavalent chromium with a mass concentration of $\gamma(Cr^{+6})$ = 500 mg/L of Cr^{+6}: Weigh 141.4 mg of potassium dichromate (see m) previously dried at 105 °C for 2 h, dissolve with water, and make up to 100 mL, 1 mL of this solution is equivalent to 500.0 µg of Cr^{+6}.

The calibration curve was carried out using the determination of hexavalent chromium in water under the official Mexican standard NMX-AA-044-SCFI-2014, which allows us to detect the presence of hexavalent chromium in water with a colorimetric method where hexavalent chromium Cr(VI) in the presence of an acidic medium gives rise to an oxidation-reduction reaction with the presence of 1,5-diphenylcarbazide, resulting in a complex red-violet color.

Having a sample with unknown composition measured by spectroscopy signal at 540 nm together with the calibration curve, allows us to know the exact composition of hexavalent chromium, since the color intensity is directly proportional to concentration.

To concentration of hexavalent chromium working reference solution γ Cr(VI) = 5 mg/L of Cr(VI), different calibration solutions were prepared with concentration of 0.1, 0.04, 0.1, 0.2, 0.3, 0.4, and 0.5 mg/L Cr(VI). In Figure 2a) the results of the absorbance data for the standard solutions generating the calibration line, and the adjustment is carried out by linear regression, obtaining an approximation with a coefficient R of 0.99996 ≈ 1 (See Figure 2b).

In accordance with the standard, the pH is adjusted to each of the samples between 9.3 and 9.7 by adding 1 mL of the buffer solution plus 0.6 mL of the 5 mol/L or 1 mol/L sodium hydroxide solution, for every 100 mL of sample to reach the pH in the indicated range, (never dilute to more than 10% of the total volume of the sample). Subsequently, adjust pH to 2.0 ± 0.5 by adding 0.25 mL (5 drops) of phosphoric acid per 100 mL, and according to the pH of the standard, use sulfuric acid. Finally, follow the procedure described for the samples for the development of color. It is important to read the absorbance of the solutions immediately.

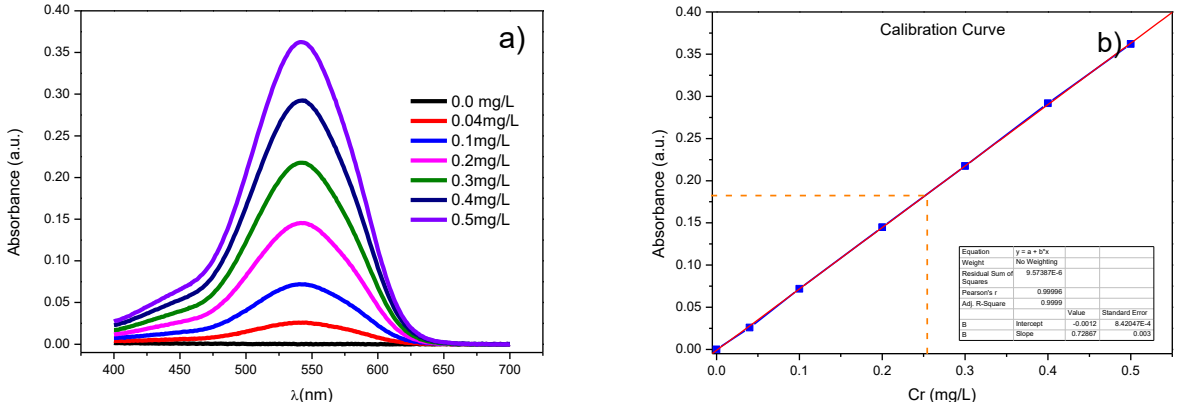


Figure 2a) Maximum absorbance of tests by the diphenylcarbazide method of the potassium dichromate molecule ($K_2Cr_2O_7$) at 540 nm of concentration ranges of 0.1, 0.04, 0.1, 0.2, 0.3, 0.4 and 0.5 mg/L and 2 b) linear regression fit of the different concentrations

To determine the Cr^{6+} content in the sample, the pH was adjusted to between 9.3 and 9.7, then to 2.0±0.5, according to the procedure described in the calibration curve steps. Finally, the diphenylcarbazide solution was added, mixed, and left for 5 to 10 minutes for complete color development. After this time, the absorbance of the samples was immediately measured using a Cary 100 spectrophotometer, monitoring the characteristic absorbance band of Cr(VI).

2.7. Flame atomic absorption (AA)

To analyze the total chromium content in the different types of samples, a PerkinElmer AAnalyst 200 Atomic Absorption Spectrometer with flame was used. The detection limit of the method is 5 ppm; therefore, a calibration curve was prepared, and dilutions of the solutions were made for proper analysis.

2.8. Point of Zero Charge

Using a rapid test, the point of zero charge (pH_{ZPC}) was determined, which refers to the pH at which the net surface charge of the material particles is zero.

To determine the pH_{PZC} of the sample, 0.05 g of the ZnMnAl adsorbent was added to each of a series of beakers containing 50 mL of a 0.1 mol/L KCl synthetic solution. Initial pH values (pHi) ranging from 2 to 9 were adjusted by adding 0.2 mol/L HCl or NaOH solutions. After 48 h of magnetic stirring at constant room temperature, the final pH (pHf) was measured using a PH 10 pH meter equipped with a P100C-BNC combination glass electrode. Using a graphical method, ΔpH (pHi − pHf) versus pHi, pH at the point of zero charge for each solid was estimated at ΔpH = 0.

2.9. Cr Adsorption Study

Adsorption tests were carried out in a glass reactor, in which 0.05 g of the ZnMnAl sample and 50 mL of a synthetic potassium dichromate solution at 40 ppm were added. Subsequently, 0.025 g of citric acid and 50 µL of phosphoric acid were introduced, achieving a pH of 2. The experiments were conducted at constant temperature and under stirring at 200 rpm. Aliquots of 3 mL were collected at intervals of 10–20 minutes. To prevent catalyst particle carryover into the solution during analysis, a syringe fitted with a nylon filter (45 µm mesh size, 2.5 cm diameter) was used. From minute 60 onward, aliquots were collected every 20 minutes until the final of the reaction, 3 hours left. Those samples were analyzed by UV–Vis spectroscopy using an Agilent Cary 100 spectrophotometer, monitoring the characteristic absorption band of this compound centered at approximately 336 nm.

Comparative systems using the ZnAl-LDH and ZnMnAl samples were evaluated to study the different parameters affecting adsorption–reducing performance, including pH, Cr concentration (adsorbate), and catalyst loading (adsorbent). The catalyst loadings investigated were 0.025, 0.05, and 0.075 g. Contact times of 20, 40, 60, 80, and up to 100 minutes were applied in some experiments. The temperature was maintained constant at 25 °C, and the initial Cr(VI) concentration was varied between 20, 40, 60, 80, 100, 150, and 200 ppm. In some tests, the aliquots obtained were analyzed by UV–Vis spectrophotometry at the end of the reaction ("at time") and after 24 hours ("after 24 h").

2.9.1. Influence of pH

The influence of pH on Cr(VI) adsorption was evaluated at room temperature (25 °C) using three different pH values: 2, 4, and 6. The solutions were adjusted by adding 0.1 mol L^{-1} NaOH or HCl and using a portable pH meter (PH 10 model) equipped with a P100C-BNC combination glass electrode. A total of 50 mL of a 40 ppm Cr(VI) solution containing 50 mg of the ZnMnAl adsorbent was kept under constant stirring for 180 min. Subsequently, filtered aliquots were withdrawn at predetermined time intervals (every 20 min) and analyzed using a previously established calibration curve at a wavelength of λ = 339 nm to determine the equilibrium concentration of Cr(VI) at each pH. Using Equation (1), the equilibrium adsorption efficiency (R%) of the synthesized material for Cr(VI) removal was calculated.

$$\%R = 100\frac{C_i - C_f}{C_i} \qquad \textit{Eq.1 ……}$$

2.9.2. Influence of concentration

The influence of the initial Cr(VI) concentration (Ci) on the adsorption process was investigated using solutions with different concentrations (20, 40, 60, 80, 100, 150, and 200 ppm) at pH 2 and a constant temperature of 25 °C. In each adsorption experiment, 50 mg of adsorbent and 50 mL of Cr(VI) solution were used. The residual Cr(VI) concentration (Ct) was determined by UV–Vis spectrophotometry (λ = 336 nm) using the Lambert–Beer law. This analysis allowed the determination of the amount of Cr(VI) adsorbed at different initial concentrations over specific time intervals. The adsorption capacity of the ZnMnAl adsorbent, expressed as the amount of Cr(VI) adsorbed (qt, in mg·g^{-1}), was calculated using Equation (2).

$$qt = \frac{C_i - C_t}{m} x\ V \qquad \textit{Eq.2……}$$

2.9.3. Influence of contact time

Under the same conditions (temperature, stirring, and pH), the influence of contact time on Cr(VI) adsorption was evaluated using 50 mg of the ZnMnAl adsorbent and 50 mL of a 40 ppm Cr(VI) solution. Aliquots were collected every 20 minutes (0, 20, 40, 60, 80, 100, 120, 140, 160, and 180 min). The amount of adsorbed Cr (qt) and the adsorption efficiency (%) were calculated using Equations (1) and (2), respectively, to assess the effect of contact time.

2.9.4. Kinetic study of adsorption

To determine the adsorption kinetics, 50 mL of a synthetic Cr (VI) solution and 50 mg of the ZnMnAl adsorbent were used at room temperature and pH 2 for 80 minutes. Aliquots were withdrawn every 20 minutes using a syringe fitted with a filter and analyzed by UV–Vis spectrophotometry. The adsorption process was evaluated using pseudo-first order and pseudo-second-order kinetic models. The linearized forms of Equations (3) and (4), representing these models, respectively, were applied. In these equations, qe and qt represent the amounts of Cr(VI) adsorbed per gram of adsorbent ($mg \cdot g^{-1}$) at equilibrium and at time t, respectively, where k_1 is the adsorption rate constant for the pseudo-first-order model (min^{-1}) and k_2 is the adsorption rate constant for the pseudo-second-order model ($g \cdot mg^{-1} \cdot min^{-1}$).

Eq.3……$\ln(q_{e-}q_t) = \ln(q_e) - k_1 t$

Eq.4 …… $\frac{1}{q_t} = \frac{1}{k_2 (q_e)^2} + \frac{1}{q_e} t$

2.9.5. Isothermal adsorption models

To determine the maximum adsorption capacity of ZnMnAl material, equilibrium adsorption data were evaluated at different initial Cr (VI) concentrations under constant temperature and stirring conditions, with a contact time of 100 minutes. The Langmuir(Rodríguez-gonz 2021) (Equation 5) and Freundlich (Equation 6)(Kecili and Hussain 2018) models were fitted to the experimental data.

Eq. 5……$\frac{C_e}{q_e} = \left(\frac{1}{q_{max}}\right) C_e + \frac{1}{K_1 \, x \, q_{max}}$

Eq. 6 ……$lnq_e = lnK_F + \frac{1}{n} lnC_e$

where qmax ($mg \cdot g^{-1}$) is the maximum adsorption capacity; K_1 ($L \cdot mg^{-1}$) is the Langmuir constant related to the affinity between the adsorbent and the adsorbate; KF [$(mg \cdot g^{-1})(L \cdot mg^{-1})^{1/n}$] is the Freundlich constant; 1/n (dimensionless) is the Freundlich exponent.

3. Results and discussion

3.1. Adsorbents characterization before Cr adsorption.

For the selection of an appropriate adsorbent, it is important to consider that its synthesis should be simple, cost-effective, efficient, and environmentally friendly. The adsorbents used for Cr(VI) removal were ZnAl hydrotalcite (ZnAl-LDH) and the biphasic synthesized material of ZnAl hydrotalcite and a mixed Mn–Al oxide ($MnAl_2O_4$)(Horsth et al. 2023). The diffraction patterns of the material in Figure 3 show the characteristic diffraction maxima of ZnAl hydrotalcite-type sheet

materials appearing at (003), (006), (111), (300), and (303), which confirm a laminar structure characteristic of these crystalline materials of the letter PDF#48-1022 Zinc Aluminum Carbonate Hydroxide Hydrate. Likewise, in the sample containing Mn, it was possible to identify the crystalline structure of the ZnAl hydrotalcites. Still, at the same time it was possible to identify additional crystallographic maxima that were interpreted as corresponding to the phase of a mixed oxide of aluminum and manganese ($MnAl_2O_4$), also known as manganese aluminate spinel (galaxite) corresponding to PDF-29-0880 crystallographic letter, it shows diffraction peaks at 18.75°, 30.80°, 36.28°, 44.11°, 48.32°, 54.75°, 58.39° and 64.17° corresponding to (111), (220), (311), (400), (331), (422), (511) and (440) indexed planes, confirming the existence of a cubic crystal structure(Khaliq et al. 2024). Therefore, forming a compound of Zn, Mn, and Al between both phases (ZnMnAl).

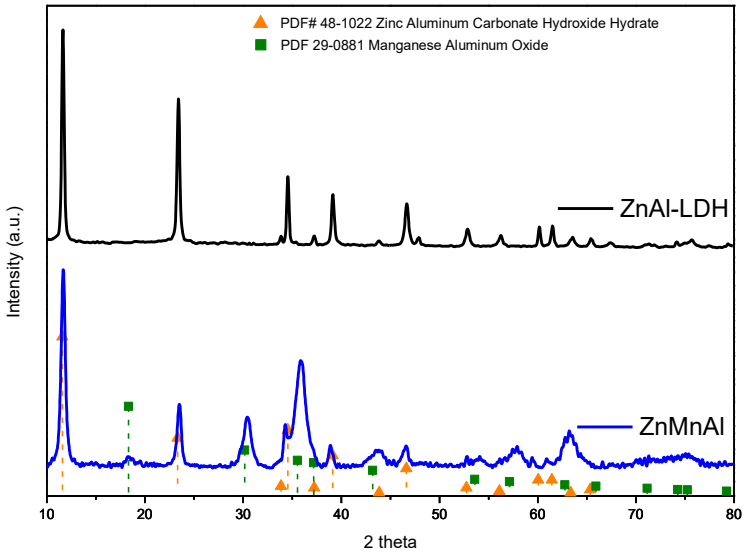
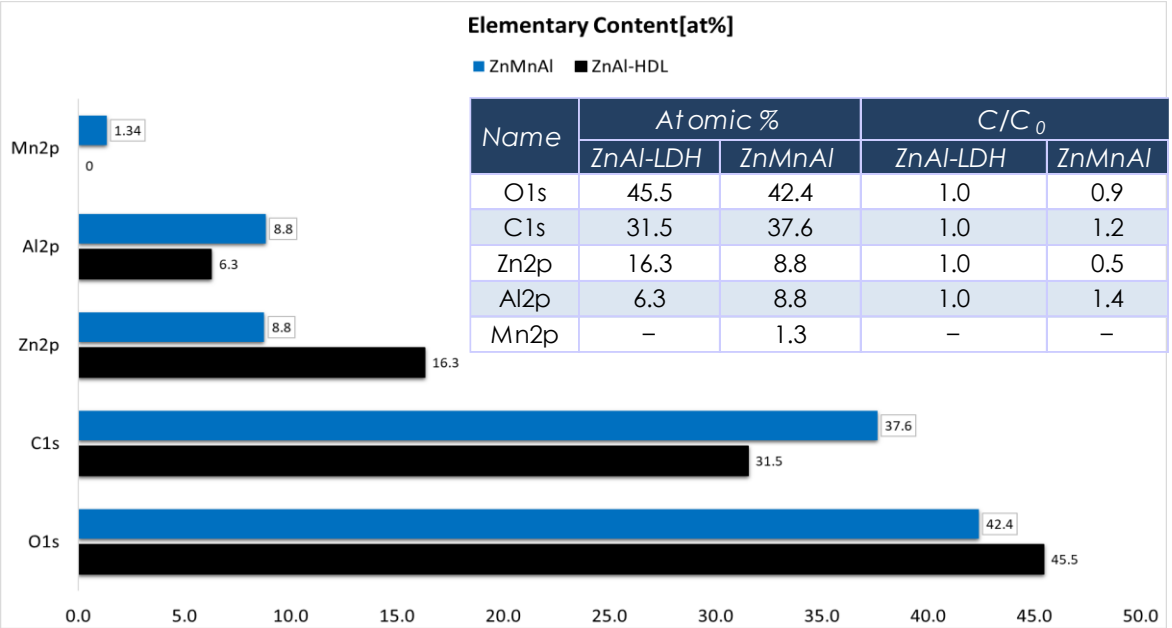


Figure 3 XRD data of (a) ZnAl LDH and (b) ZnMnAl (biphasic material) Mn_2AlO_4 and ZnAl LDH) before adsorption Cr(VI).

Based on the X-ray diffraction results shown in Figure 3, together with the XPS results shown in Figures 4 and 5a, b, c and d, several conclusions can be drawn.

Figure 4 presents complementary elements, which also suggests that carbon increases in the ZnMnAl material due to the formation of a more amorphous surface, typical of materials containing Mn–Al oxide phases. The increase in $C/C_o > 1$ confirms surface carbon enrichment in the modified material. The increase in Al content in the ZnMnAl sample is related to the formation of Mn–Al mixed oxides, since these phases expose a higher number of Al–O groups at the surface. The C/C_o value of 1.4 indicates significant aluminum enrichment at the surface.



Name	Atomic %		C/C 0	
	ZnAl-LDH	ZnMnAl	ZnAl-LDH	ZnMnAl
O1s	45.5	42.4	1.0	0.9
C1s	31.5	37.6	1.0	1.2
Zn2p	16.3	8.8	1.0	0.5
Al2p	6.3	8.8	1.0	1.4
Mn2p	–	1.3	–	–

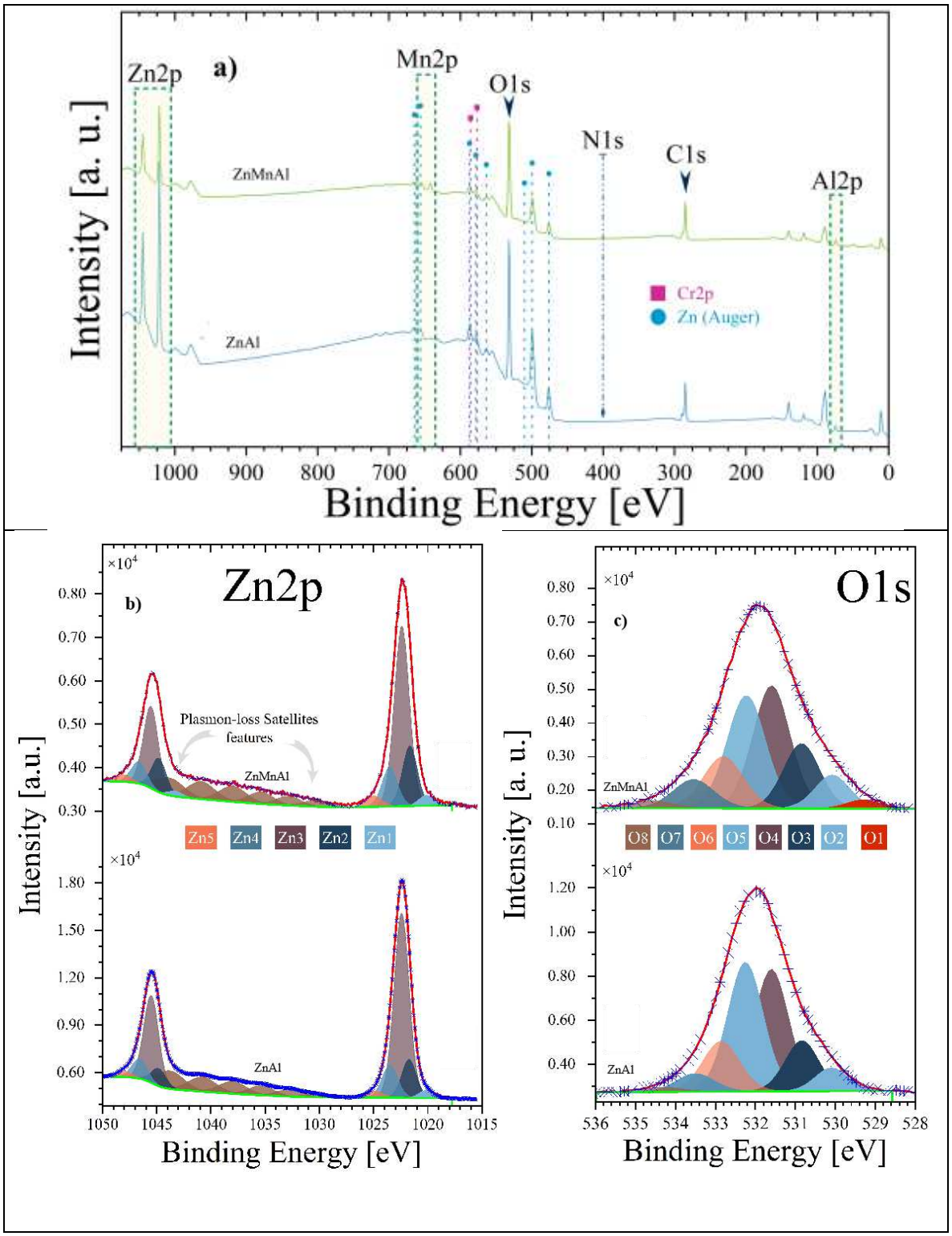
Figure 4. Atomic percentage values determined by XPS for each element present on the surface and the surface concentration ratio C/C_0 for each element in the ZnAl-LDH and ZnMnAl materials.

Additionally, according to Figure 5a), and to the calculated composition used for the synthesis of ZnAl-LDH with a 3/1 molar ratio, the actual surface Zn–Al composition exhibits a very similar ratio (5/2/1) to the calculated one. In the case of the ZnMnAl material, manganese was incorporated, leading to the formation of a new phase (a manganese–aluminum mixed oxide). The calculated molar ratio (2/1/1) for the biphasic material did not match the surface composition obtained (1/1/1/6), as shown in Figure 4.

The high-resolution XPS spectrum of Zn 2p in Figure 5b) showed two typical fitted peaks (Zn $2p_1/_2$ and Zn $2p_3/_2$) at binding energies of 1045.07 eV and 1022.02 eV, respectively, corresponding to Zn^{2+}–O bonding(Li et al. 2021; Qi et al. 2024). The C/C_0 value of 0.5 for the Zn ratio indicates a decrease of this element to half of its surface concentration in the presence of Mn, as shown in Figure 4b), providing clear evidence of surface substitution due to the presence of Mn.

In Figure 5c) the O 1s spectrum in the region around 529–535 eV was deconvoluted into three overlapping O 1s peaks corresponding to different oxygen species: oxygen oxide (O^{2-}), with a fitted peak at a binding energy of 530.49 eV, attributed to typical M–O bonding resulting from the substitution of hydroxyl groups by surface hydroxides or surface metal atoms; hydroxyl groups (–OH) from adsorbed water (H_2O), with a peak observed at a binding energy of 531.27 eV; and C–O species at 532.3 eV, as shown in Figure 4c). This latter region decreases due to the coverage of surface –OH groups on the hydrotalcite layers because of chemical modification caused by the surface formation of Mn–Al oxides, which in turn alters the morphology of the pristine material (ZnAl-LDH), as observed in Figure 5. Oxygen is the dominant element on both surfaces (ZnAl and ZnMnAl) due to the hydroxylated nature of hydrotalcites and the presence of oxides. In the ZnMnAl sample, the atomic percentage of O slightly decreases, which is consistent with manganese incorporation and the relative increase of other elements (C and Al).

Finally, at high binding energies in the range of 640–645 eV, the Mn-containing sample exhibits an increase in intensity corresponding to the Mn 2p region at 642.17 eV in Figure 5d), which is associated with Mn^{2+}, Mn^{3+}, and Mn^{4+} oxidation states, favorably contributing to both oxidation and reduction processes(Nguyen et al. 2022; Sun et al. 2023; Wu et al. 2020; Zhu et al. 2024). The low-binding-energy peak at 640.7 eV can be assigned to Mn(II), characteristic of Mn in MnO. (Nesbitt and Banerjee 1998). Manganese is present exclusively in the ZnMnAl material, confirming the formation of the Mn–Al phase (galaxite or mixed oxides), although its atomic percentage is lower than that of Zn or Al.


a)
Zn2p
Mn2p
O1s
N1s
C1s
Al2p
ZnMnAl
ZnAl
Cr2p
Zn (Auger)
Intensity [a. u.]
Binding Energy [eV]
b)
Zn2p
Plasmon-loss Satellites features
ZnMnAl
ZnAl
Zn5
Zn4
Zn3
Zn2
Zn1
Intensity [a.u.]
Binding Energy [eV]
c)
O1s
ZnMnAl
ZnAl
O8
O7
O6
O5
O4
O3
O2
O1
Intensity [a. u.]
Binding Energy [eV]

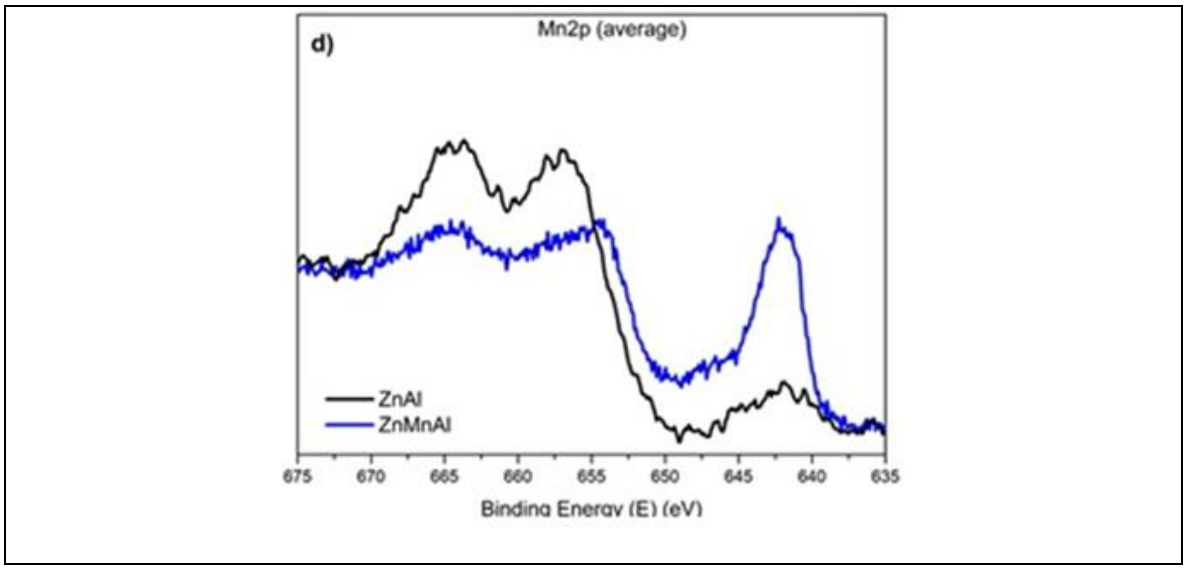


Figure 5 Comparisons of XPS results of a) general spectra b) Zn2p, c) O1s, and d) Mn2p of the ZnAl-LDH and ZnMnAl samples.

SEM images were obtained to analyze the morphology and structure of the ZnAl-LDH and ZnMnAl samples. Figure 6a) shows magnifications of 1500X and 10,000X, where nanosheets with a flake-like morphology forming agglomerates can be identified, corresponding to the pristine ZnAl-LDH sample. However, for the Mn-containing sample, Figure 6b) reveals compact solids with irregular shapes and sizes ranging from 1 to 10 µm, suggesting that Mn likely coats the layers, resulting in a smoother surface.

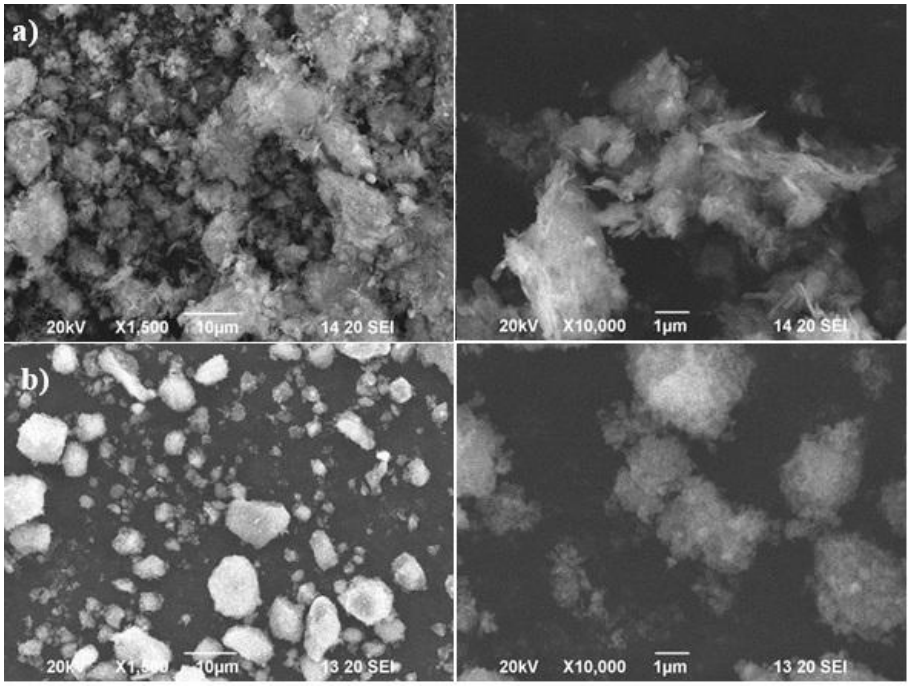


Figure 6 SEM images of a) ZnAl-LDH to 1500X and 10000X and b) ZnMnAl1 to 1500X and 10000X before adsorption evaluation.

At the same time, the FTIR spectrum of the ZnAl hydrotalcite and ZnMnAl compound before adsorption, shown in Figure 7, showed several prominent peaks characteristic of layered double hydroxides and mixed oxides. A broad and intense band at 3425 cm^{-1} is attributed to O-H vibrations of stretching of the hydroxyl groups of the HDL layers, as well as the water molecules present in the intermediate layer. The faint bands appearing in regions around 2332 y 1650 cm^{-1} are characteristics of triple and double bonds C-C, C-O, and C-N, respectively. The peak at 1355 cm^{-1} was assigned to the species CO_3^{2-} in the intermediate layer of the 2D hydrotalcite nanosheets, possibly due to the introduction of CO_2 through the dissociation of urea during the synthesis process (Madhusudan et al. 2023; Zhang et al. 2022). The bands in low frequency region (663, 552, and 448 cm^{-1}) are ascribed to the stretching vibrations of M−O and O–M–O (M = Mn, Zn, Al)(Guo et al. 2012; Palacio et al. 2010)

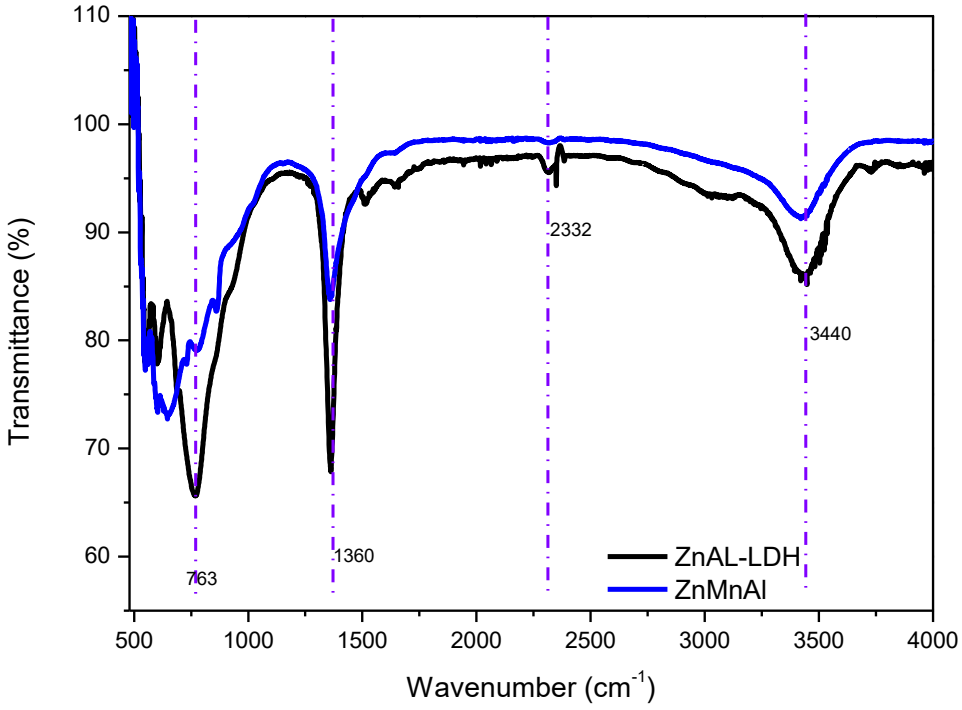


Figure 7 FT-IR spectra of the ZnAl-LDH and ZnMnAl before adsorption evaluation.

Since the adsorption capacity depends on the surface area and pore structure of the material, the efficiency may be limited by accessibility to macro- or micropores and by the volume of accessible pores of different sizes and shapes. Therefore, it was necessary to determine the sorption isotherms, which are shown in Figure 8 and correspond to type IV isotherms according to the IUPAC classification(Donohue and Aranovich 1998; Gökırmak and Gülcan 2023); these isotherms are characteristic of layered materials and mesoporous adsorbents (BET, pore diameter ~5 nm), where the adsorption behavior initially resembles that of a type II isotherm in the monolayer–multilayer region, governed by adsorbate–adsorbent interactions and interactions among molecules in the condensed state. The H3-type hysteresis loop was characteristic of both materials and was mainly formed at high relative pressures due to capillary condensation associated with irregular pore shapes, indicating the presence of mesopores in the structure.

The material composed of hydrotalcite and mixed oxides (galaxite) promoted an increase in surface area from 27.78 m^2/g for ZnAl hydrotalcite to 39.34 m^2/g for the ZnMnAl composite. This increase is associated with the formation of a new Mn–Al mixed oxide phase, which generates rougher surfaces and greater exposure of Mn active sites, and consequently leads to a decrease in pore volume (from 0.062 to 0.055 cm^3/g), related to a redistribution of porosity (see Figures 3 and 6). In this process, part of the mesopores becomes smaller due to the incorporation of oxide phases, reflecting the transition from a more layered material, such as hydrotalcites, to a more compact and heterogeneous solid (ZnMnAl), which tends to partially block or fill pore channels.

For the biphasic ZnMnAl material, the adsorption–desorption curve shows a more pronounced increase at high relative pressures ($P/P_o > 0.8$), indicating greater accessibility to meso–macroporous pores.

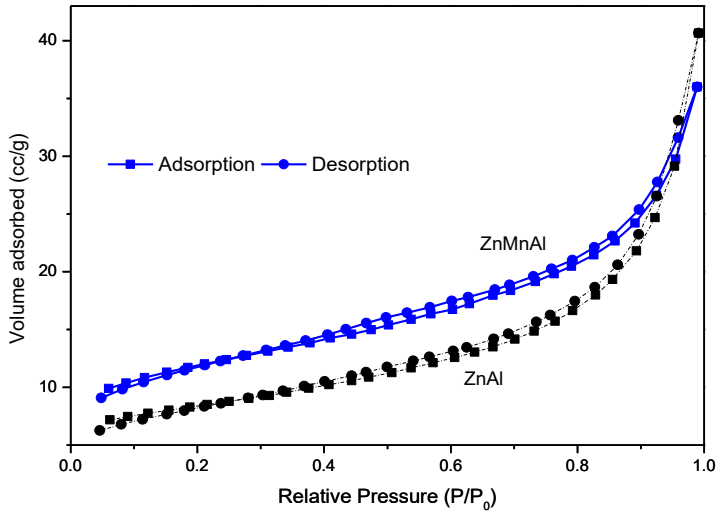


Figure 8. Adsorption–desorption isotherms of nitrogen for the samples of ZnAl-LDH and ZnMnAl biphasic material.

Using a graphical method, ΔpH ($pH_i - pH_f$) versus pH_i (Figure 9), the pH at the point of zero charge (PZC) for the sample was determined from the intersection at $\Delta pH = 0$, close to 6.7. This indicates that below this value (PZC < 6.7), the adsorbent surface acquires a positive surface charge due to protonation of nitrate groups and the dissociation of H^+. Above 6.7 (PZC > 6.7), a negative surface charge tends to develop due to deprotonation of hydroxyl groups (OH^-).

Because ions are present in the medium as products of salt dissociation (charge carriers), specific chemical adsorption occurs. Since the ZnMnAl adsorbent material is positively charged due to protonation of surface hydroxyl groups, electrostatic attraction toward oxygen-containing anions such as $HCrO_4^-$ and CrO_4^{2-} is enhanced, facilitating Cr(VI) removal through the adsorption process. As the pH approaches the PZC (~6.7), the surface becomes nearly neutral and anionic adsorption decreases markedly; above this value, the surface becomes predominantly negative, generating electrostatic repulsion that almost completely inhibits the adsorption process.

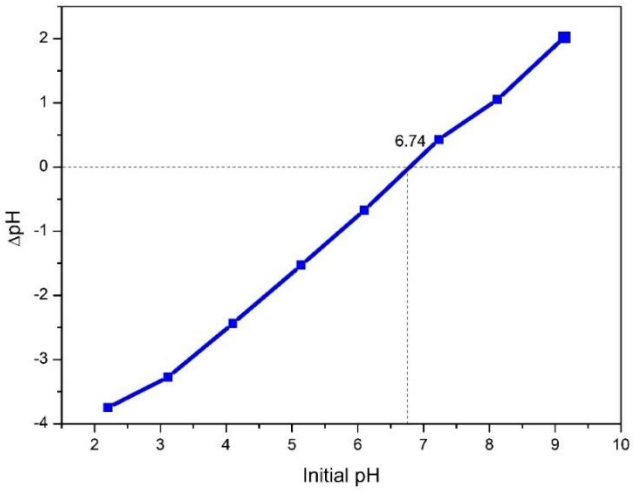


Figure 9. pHPZC analysis of the ZnAl-LDH and ZnMnal biphasic material.

2.1. Adsorption experiments

The initial Cr(VI) adsorption tests were carried out using 0.05 g of ZnAl-LDH or ZnMnAl as adsorbents for comparison, in 50 mL of a synthetic potassium dichromate solution at 40 ppm and pH 2. Specifically, 0.05 g of the ZnMnAl compound was placed in a glass beaker under constant stirring at room temperature for 180 min, and 3 mL aliquots were withdrawn using a syringe fitted with a filter. Aliquots were collected every 20 minutes. Figure 10a) shows the UV–Vis spectroscopic analysis results at the end of the evaluation in terms of qt, while Figure 10b) presents the results of the same aliquots after 24 hours. For the different measurement times, ZnAl-LDH hydrotalcite-type materials did not exhibit Cr(VI) adsorption; however, for the Mn-containing sample (ZnMnAl), the adsorption–reducing efficiency for chromium exceeded 95%.

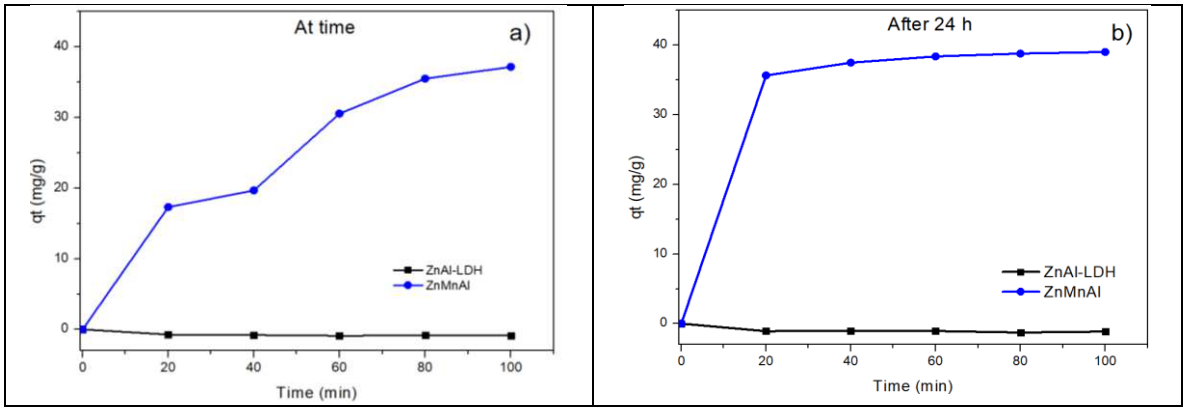


Figure 10. Effect of Mn on ZnAL-LDH (ZnMnAl biphasic material) for Cr(VI) to 40 ppm adsorption, analyzed a) over time and b) after 24 hours.

Figure 11a) shows that the time required to reach equilibrium for the aliquots evaluated with the biphasic ZnMnAl material, which acts as both an adsorbent and a reducing agent for Cr(VI), differs notably when comparing the measurements taken at the end of the reaction and those recorded after 24 h (Figure 11b). It is important to note that the same aliquots were analyzed in both cases. The measurements described as “at time” correspond to aliquots evaluated immediately after completion of the reaction, whereas the “after 24 h” measurements correspond to those same aliquots reanalyzed after standing for 24 h. This additional analysis was performed because, after removing the photocatalyst, gradual decolorization was still observed in the aliquots over time, suggesting the possible occurrence of ongoing or chain reactions in solution.

Therefore, UV–Vis measurements were carried out again to verify whether further reactions continued to take place. For the initial measurement, equilibrium was reached at approximately 100 min, whereas in the measurements performed after 24 h, equilibrium was reached within only 10 min.

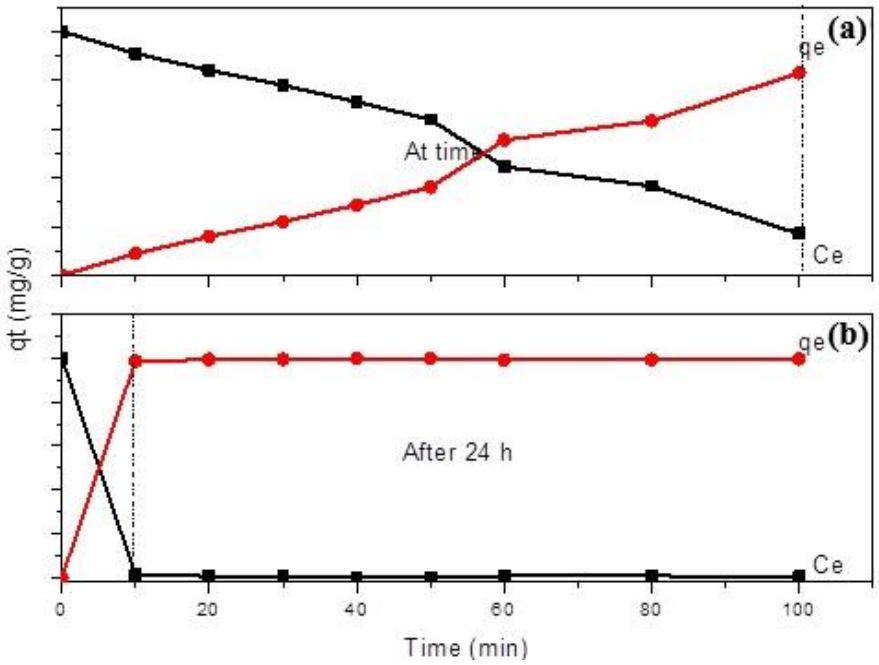


Figure 11 Analysis of the effect of equilibrium for the ZnMnAl biphasic material on 40 ppm Cr (VI) adsorption, a) at time and b) after 24 hours.

To study the effect of pH on Cr(VI) adsorption for the ZnAl-LDH sample in comparison with the modified ZnMnAl sample, several experiments were carried out at pH values of 2, 4, and 6. Figure 12a) shows the results of the amount of Cr(VI) adsorbed, obtained by UV analysis of each aliquot at the time of sampling, while Figure 12b) presents the results after 24 hours of resting. It was determined that at pH 2 the highest Cr adsorption efficiency was achieved, reaching up to 90%, whereas at pH 4 and 6 the adsorption capacity reached only 13% and 0%, respectively, after 180 minutes. In contrast, for samples allowed to rest for 24 hours, the results showed that after 20 minutes the adsorption capacities were 97%, 73%, and 85% for pH 2, 4, and 6, respectively.

At pH 2, the material exhibits maximum protonation, generating a high density of positive charges on the surface. This promotes electrostatic interaction with the predominant Cr(VI) species, mainly

$HCrO_4^-$(Tan et al, 2022), facilitating specific adsorption through surface complex formation and increasing the proximity of the anion to Mn redox centers.

The observed adsorption–reducing behavior is closely correlated with the surface charge of the material, as inferred from the point of zero charge (PZC ≈ 6.7). Below this value, the solid surface is positively charged, which favors the electrostatic attraction of anionic Cr(VI) species.

The experimental results show that the process efficiency is maximized at pH 2, reaching equilibrium within 20 minutes, and progressively decreases with increasing pH due to possible competition and desorption effects. This behavior can be explained by a combination of factors associated with both Cr(VI) speciation and the surface characteristics of the adsorbent.

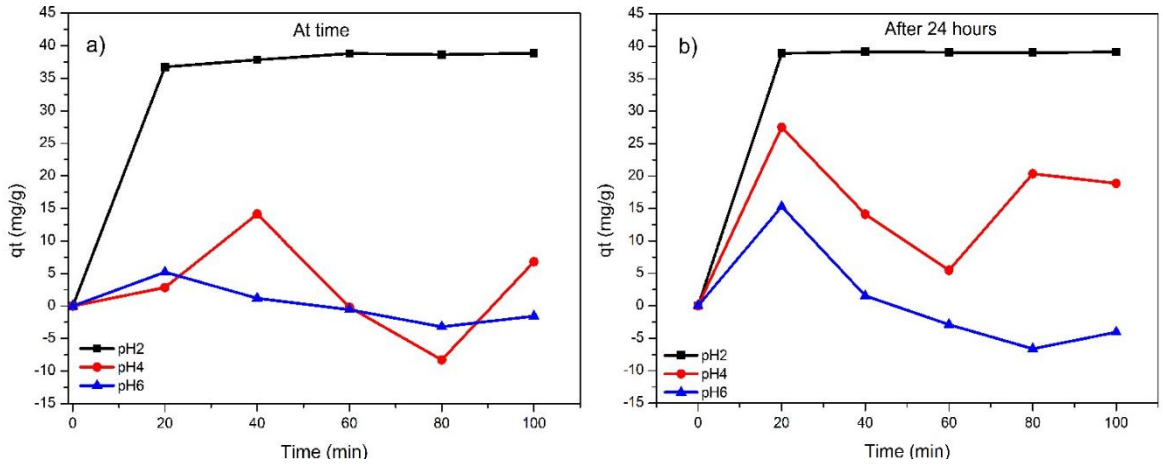


Figure 12 Cr(VI) removal rate at different pH (2, 4, and 6) with ZnMnAl, a) at time and b) after 24 hours.

To determine the optimal adsorbent loading that yields the highest Cr(VI) adsorption efficiency at pH 2 and room temperature, adsorption experiments were carried out using 25, 50, and 75 mg of the ZnMnAl composite. According to Figure 13a), the best adsorption performance was achieved when a loading of 50 mg was used, reaching efficiencies higher than 97% after 100 minutes, while Figure 13b) shows efficiencies above 99% within 20 minutes. When loadings higher than 75 mg are employed, saturation of the adsorbent occurs, leading to competition among the active sites of the material. This competition generates attractive forces in different directions that interact with the adsorbate, resulting in a decrease in Cr(VI) adsorption efficiency.

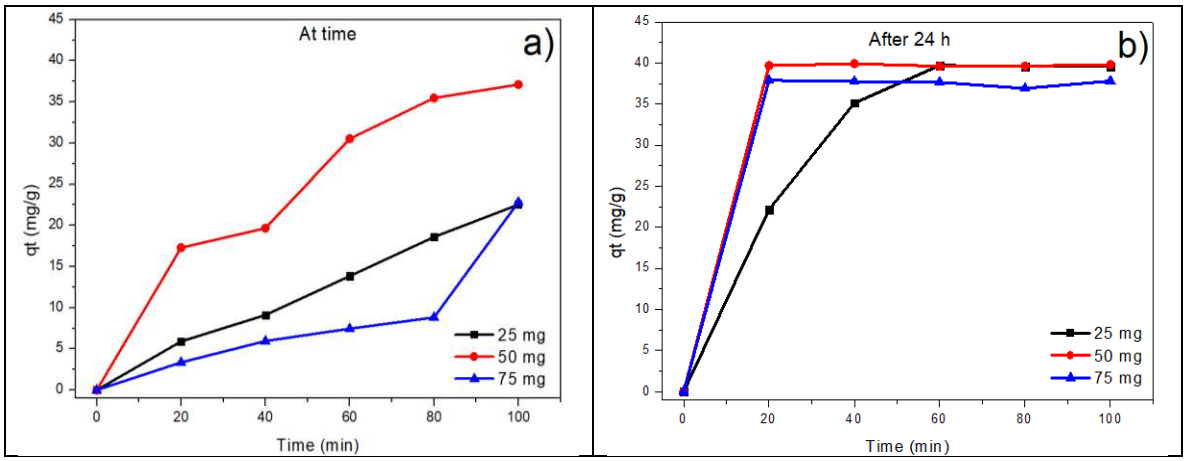


Figure 13 Effect of different Adsorbent dosages of ZnMnAl biphasic material (25, 50, and 75 mg) on Cr (VI) removal rate, a) at time and b) after 24 hours.

Experiments were carried out at a constant pH of 2 and at different Cr(VI) concentrations (20, 40, 60, 80, 100, 150, and 200 ppm). As shown in Figure 14a), the time required to reach equilibrium for the aliquots measured immediately was shorter than 100 min; however, adsorption efficiencies higher than 80% were not achieved within 80 min of contact between the adsorbate and the adsorbent. In contrast, the same aliquots that were allowed to stand for 24 h reached equilibrium within only 20 min, achieving efficiencies higher than 90% for all Cr(VI) concentrations (see Figure 14b).

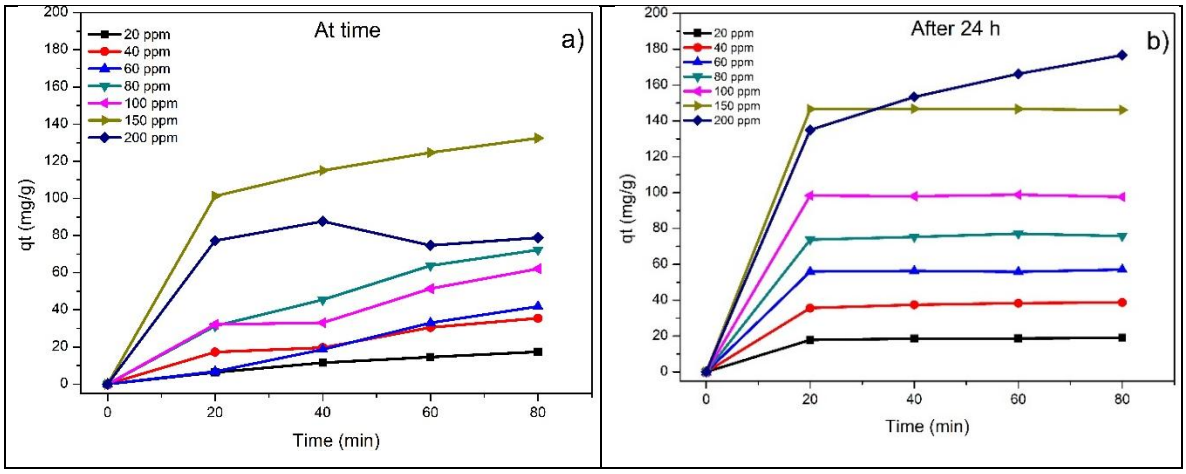


Figure 14. Cr(VI) removal rate at different concentrations (20, 40, 60, 80, 100, 150 and 200 ppm) with ZnMnAl biphasic material, a) at time and b) after 24 hours.

2.2. Kinetic study of adsorption

Pseudo-first- and pseudo-second-order model (k_1, R^2) "at time"

The results of the pseudo-first-order (Figure 15a) and pseudo-second-order (Figure 15b) kinetic models corresponding to the adsorption of the ZnMnAl composite at different Cr(VI) concentrations (20, 40, 60, 80, 100, 150, and 200 $mg \cdot L^{-1}$) show favorable behavior throughout the entire evaluation

period; however, a better fitting is obtained when using the measurement values collected after 24 h following filtration (Figure 16 a and b).

The calculated R^2 values for each model are listed in Table 1, showing that fitting is depending on the solution concentration. It is observed that at very low and high concentrations (20 ppm and ≥150 ppm), the pseudo-second-order model provides a better fit (R^2 ≈ 0.98–0.997), whereas for concentrations between 40 and 100 ppm, the pseudo-first-order model shows a better correlation. Nevertheless, the pseudo-first-order model can be considered to provide a more consistent overall fitting.

These results confirm that the adsorption mechanism, at least in the initial stage, changes with concentration: it is predominantly chemical (second order) at low and high Cr(VI) doses, while diffusion-controlled or physical adsorption processes (first order) dominate at intermediate concentrations.

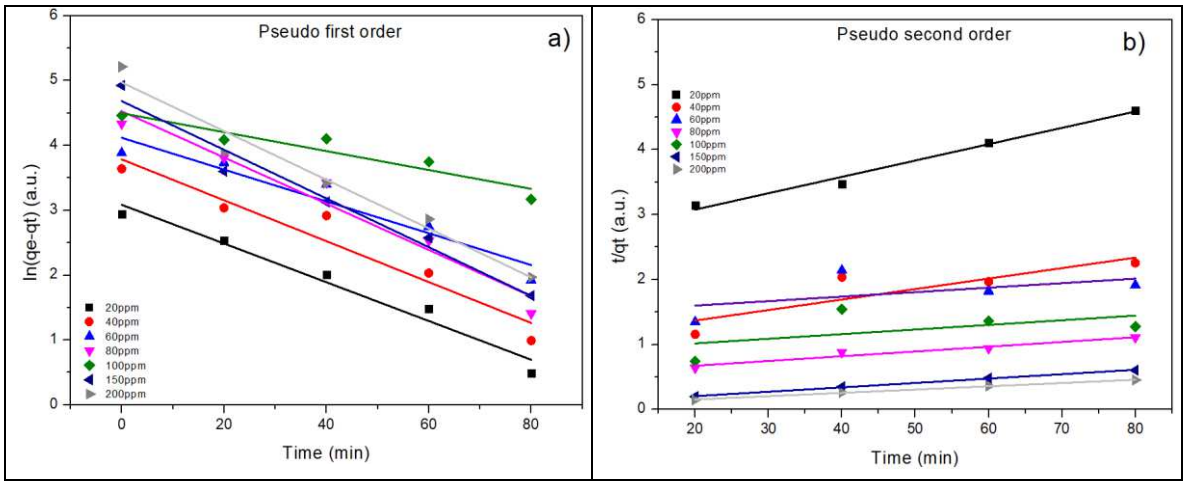


Figure 15 a) Pseudo-first and b) second order "at time" model of Cr(VI) at different concentrations (20, 40, 60, 80, 100, 150, and 200 ppm) with the ZnMnAl biphasic material.

Table 1. Parameters of the first order and second-order kinetic models for the adsorption of Cr(VI) onto ZnMnAl compound at time.

Solution concentration (ppm)	Pseudo-first order at time			Pseudo second order at time		
	qe1 (mg g^{-1})	k1	R^2	qe2 (mg g^{-1})	k2	R^2
20	17.37	0.0298	0.9597	39.74	2.460E-04	0.98023
40	35.48	0.0315	0.9114	61.95	2.490E-04	0.62747
60	41.79	0.0245	0.8975	144.71	3.270E-05	-0.07321
80	72.25	0.0356	0.9407	136.61	1.019E-04	0.92645
100	68.56	0.0145	0.8676	140.252	5.816E-07	0.07194
150	132.50	0.0375	0.9558	147.92	7.678E-04	0.99686
200	176.66	0.0375	0.9558	197.23	4.930E-04	0.99686

Pseudo-first- and pseudo-second-order model (k_1, R^2) "After 24 h"

The results obtained for the pseudo-first-order model after 24 h, summarized in Table 2, indicate that the R^2 values fluctuate significantly when compared with those of the pseudo-second-order model. The pseudo-first-order model, shown in Figure 16 a), does not adequately describe the adsorption process at most concentrations, providing acceptable fits only at 80 ppm (R^2 = 0.9680) and 100 ppm (R^2 = 0.9493). In contrast, the pseudo-second-order model presented in Figure 16 b) exhibits a more favorable fitting behavior (see Table 2), with consistently high R^2 values, achieving in some cases an almost perfect fit of the experimental data (R^2 = 1).

Therefore, these results suggest that the adsorption process after 24 h is predominantly governed by a chemical mechanism (chemisorption), likely involving the formation of specific bonds or electron-transfer interactions with Cr(VI).

The k_1 values vary considerably (from 0.0112 to 0.1447), indicating a large dispersion in the initial adsorption rate. In contrast, the k_2 values fall within the range of 4.798×10^{-4} to 1.953×10^{-1}. Notably, higher k_2 values at certain concentrations (e.g., 150 ppm with $k_2 = 1.953 \times 10^{-1}$) indicate that adsorption efficiency is strongly concentration-dependent, possibly due to a greater availability of Cr(VI) ions to occupy the active sites of the adsorbent.

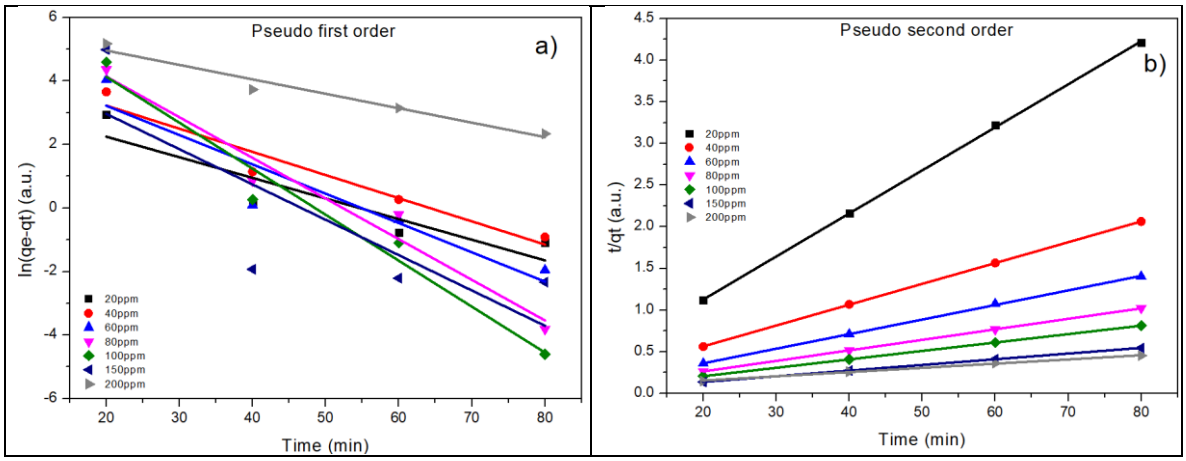


Figure 16 a) Pseudo-first and b) second order "after 24 h" model of Cr(VI) at different concentrations (20, 40, 60, 80, 100, 150, and 200 ppm) with the ZnMnAl biphasic material.

Table 2 Parameters of the first order and second-order kinetic models for the adsorption of Cr(VI) onto ZnMnAl compound "after 24 h"

Solution concentration (ppm)	Pseudo first order after 24 hours			Pseudo-second order after 24 hours		
	qe (mg g^{-1})	k1	R^2	qe (mg g^{-1})	k2	R^2
20	18.99	0.0640	0.7514	19.34	2.874E-02	0.9977
40	38.76	0.0729	0.9157	40.00	9.843E-03	0.9999
60	57.06	0.0922	0.8101	57.14	2.759E-02	0.9993
80	77.29	0.0127	0.9680	79.36	1.498E-02	0.9999
100	98.41	0.1447	0.9493	99.00	3.000E-02	1.0000
150	146.10	0.0112	0.4670	146.84	1.953E-01	1.0000
200	176.66	0.0454	0.9438	200	4.798E-04	0.9968

The values obtained after 24 h appear to be underestimated in pseudo-first-order kinetics, since the experimental data do not follow a straight line in the ln(qe − qt) vs. t plot; therefore, an adequate fit is not achieved.

Comparison of pseudo-first and pseudo second order kinetic models ("at the moment" and "after 24 h")

The adsorption kinetics of Cr(VI) onto the ZnMnAl composite were analyzed using pseudo-first- and pseudo-second-order models at initial concentrations of 20, 40, 60, 80, 100, 150, and 200 $mg \cdot L^{-1}$. Immediate measurements ("at time") showed that both models reasonably describe the adsorption process (Figure 15a and b), but the best fitting was obtained from aliquots analyzed after 24 h of standing following filtration (Figure 1a and b), indicating that slower surface processes contribute to the overall adsorption efficiency.

R^2 values for each model, summarized in Tables 2 and 3, reveal a dependence on Cr(VI) concentration. For very low (20 ppm) and high concentrations (≥150 ppm), the pseudo-second-order model provides the best fit ($R^2 \approx 0.98–1.00$), suggesting that chemisorption dominates. For intermediate concentrations (40–100 ppm), the pseudo-first-order model fits better, indicating that diffusion-controlled or physical adsorption processes are more relevant. This shift in mechanism with concentration suggests that, initially, adsorption involves both diffusion and surface interactions, while at longer times, chemical interactions dominate.

The kinetic constants further support this interpretation. The k_1 values ("at time") vary widely, reflecting differences in initial adsorption rates, while k_2 values ("after 24 h") are consistently higher at certain concentrations (e.g., 150 ppm), indicating that the adsorption efficiency depends on the availability of Cr(VI) to occupy active sites. These observations are consistent with a redox-assisted adsorption mechanism: Mn centers in the ZnMnAl material undergo electron transfer, facilitating the reduction of Cr(VI) and stabilizing its adsorption on the surface. Consequently, the combination of chemisorption and Mn-mediated redox reactions enhances the overall removal efficiency, particularly at higher contact times.

2.3. Isothermal adsorption models

To delve deeper into the nature of the interaction between the adsorbate and the adsorbent, the experimental adsorption data were fitted to the Langmuir and the Freundlich isotherm models.

The Langmuir model showed in Figure 17 a) the best experimental fit ($R^2 = 0.8306$), suggesting that chromium adsorption occurs predominantly in a monolayer on homogeneous active sites of the material. This behavior is characteristic of surfaces with well-defined adsorption centers, associated with structural hydroxyl groups and Mn–O metal sites.

The high maximum capacity value, qmax = 232.56 $mg\ g^{-1}$, indicates a high density of active sites available for chromium retention. This result confirms the remarkable efficiency of the biphasic material for metal removal, exceeding values reported for many conventional adsorbents.

The constant KL = 0.1458 $L\ mg^{-1}$ reflects a moderate-to-high affinity between the adsorbate and the adsorbent. This value suggests that the interactions are not exclusively physical, but involve significant chemical contributions, such as surface complexation or direct bonding with atoms on

the adsorbent surface, generally through covalent or coordinate bonds between chromate species and functional groups of the solid.

However, the Freundlich model showed a lower fit (R^2 = 0.6283) in Figure 17 b), indicating that, although surface heterogeneity exists, this model describes the process less accurately than Langmuir. Nevertheless, the obtained parameters provide relevant information about the energetic nature of the surface.

The value n = 1.603 (with 1/n = 0.623) indicates that adsorption is favorable and that the interactions between the chromium and the material surface are relatively strong. Values of n > 1 are usually associated with processes dominated by partial chemisorption or specific interactions between the adsorbate and the active sites.

The constant KF=0.1844 shows the presence of multiple types of adsorption sites with different energies, which is consistent with the biphasic nature of the material, where hydrotalcite domains and MnAl oxide regions with different chemical properties coexist.

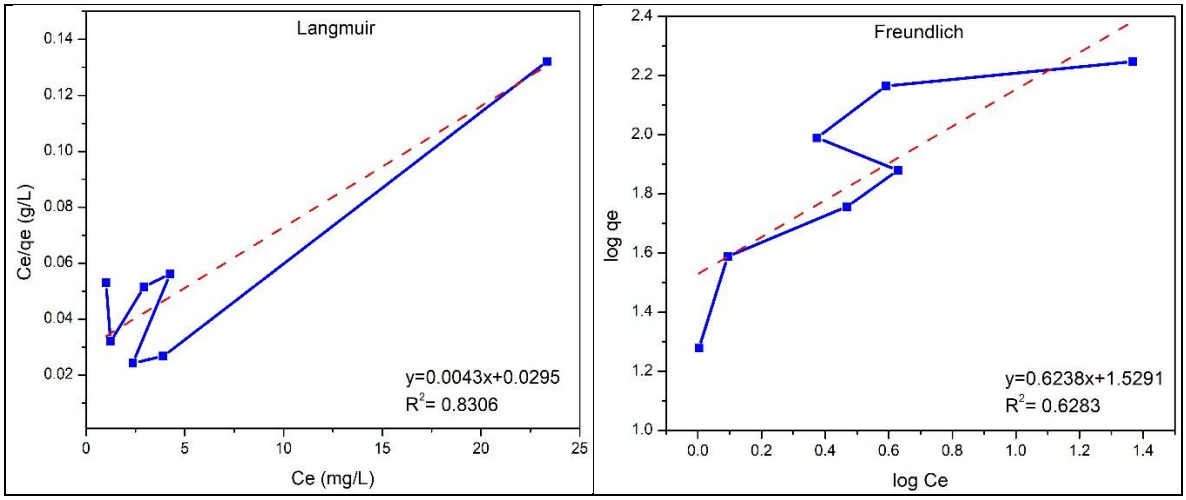


Figure 17 Isothermal first for the adsorption removal of Cr(VI) onto ZnMnAl (a) Langmuir, and (b) Freundlich

In addition, as a prototype for the implementation of the adsorbent material, pellets were used to improve and facilitate their incorporation into conventional water treatment processes. This configuration offers significant operational and environmental advantages due to the ease of material recovery, minimizing particle loss by drag, and reducing the need for additional filtration or centrifugation steps. Furthermore, it enables potential pilot- or industrial-scale applications using fewer complex processes and allows for the reuse of the reducing adsorbent material.

For this purpose, a compact pellet of the ZnMnAl composite was prepared. A mass of 0.1 g of the adsorbent material was weighed and, using a mold and a hydraulic press, a pressure of 1 ton was applied. The resulting pellet (Figure 18a) was immersed in a 40 ppm Cr (VI) solution. Aliquots were analyzed by UV–Vis spectroscopy at the end of the adsorption process (3 h) and after 24 h, with the results shown in Figure 18b). After 180 min of contact, approximately 22% of Cr (VI) was removed; however, after 24 h, the removal efficiency increased significantly, reaching up to 99% from 140 min onward.

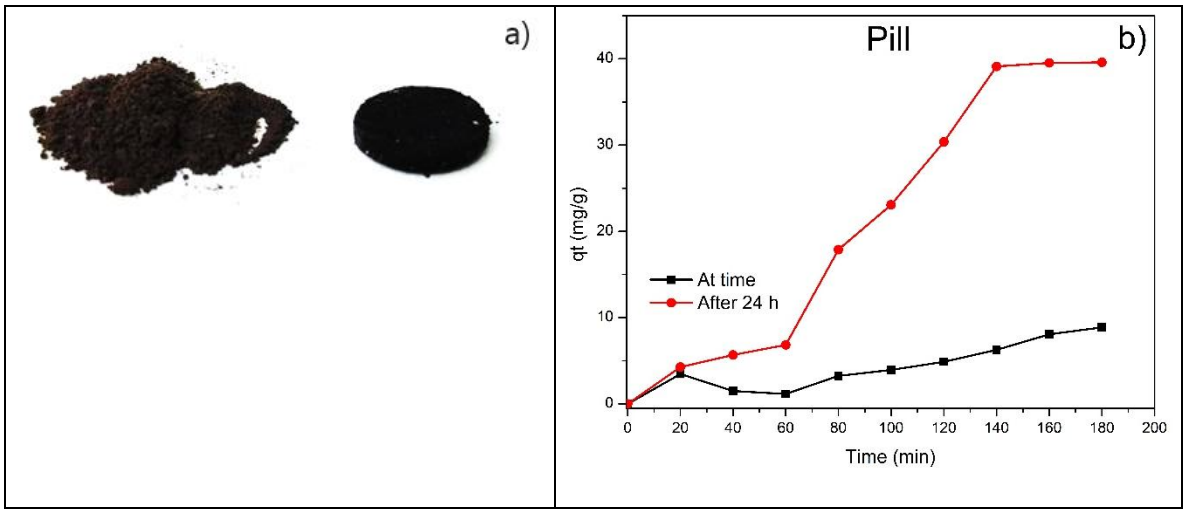


Figure 18 a) ZnMnAl pill and b) UV spectroscopy results of the aliquots obtained in the adsorption of chromium VI with ZnMnAl in the form of a pill were evaluated at the time and after 24 hours.

Reuse cycles were carried out using a ZnMnAl composite pellet as the adsorbent under the standard conditions employed in previous tests, but at a higher potassium dichromate concentration (100 ppm). An aliquot was taken at the beginning of each experiment and another at the end (after 24 h) of each evaluation. In every cycle, the initial potassium dichromate solution concentration was 100 ppm, and the same pellet was reused in all cycles without any prior regeneration treatment. The C/C_o removal efficiencies of the seven cycles were compared in a single plot (see Figure 19), showing that all cycles achieved efficiencies higher than 95%.

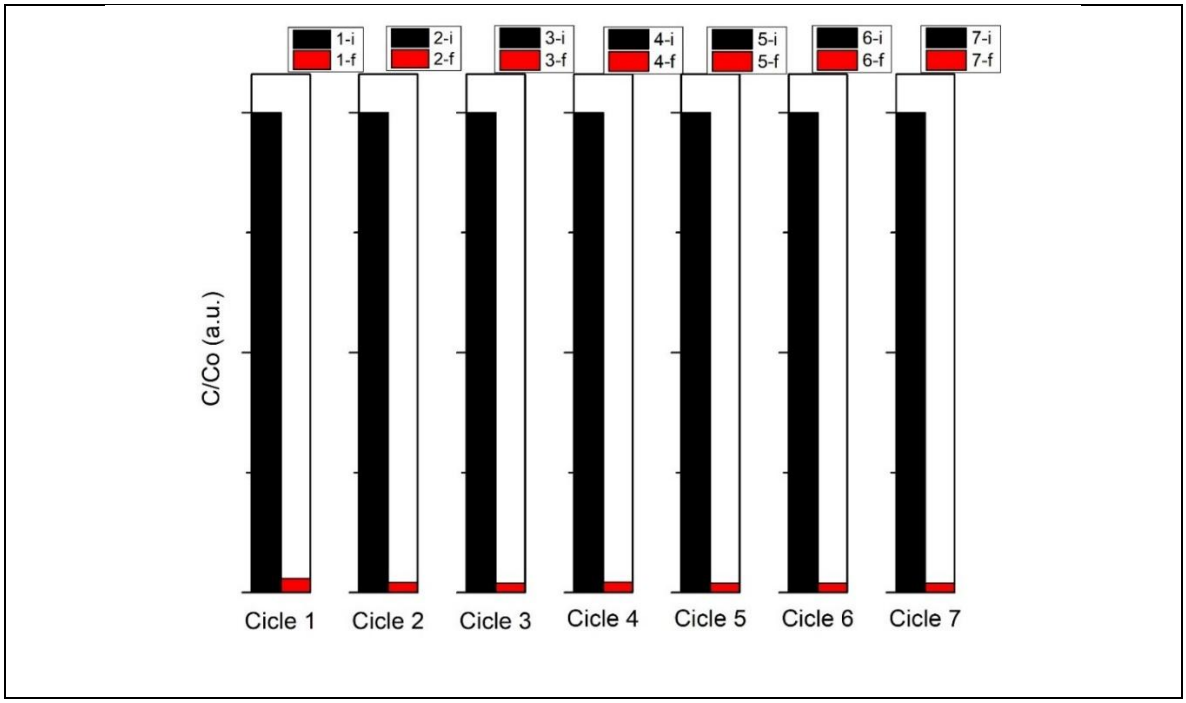


Figure 19. Comparison of C/Co of cycles using the same pill

3.2. Discussion of results after chromium adsorption tests

XRD results suggest that Cr (VI) removal involves a coupled adsorption–reduction process occurring at the solid–solution interface. ZnAl-LDH phase mainly provides adsorption sites and structural modulation under acidic conditions, while the $MnAl_2O_4$ phase serves as the redox-active component facilitating electron transfer for Cr(VI) reduction, evidencing the synergistic functionality of the bifunctional ZnMnAl material.

Figure 20a) shows the characteristic X-ray diffraction results of the ZnMnAl material before and after the adsorption evaluation. After Cr adsorption, a restructuring was observed in the hydrotalcite phase due to the loss of Zn and Al observed by XPS. This loss resulted from the dissolution (loss in the lamellar structure) of the smaller crystallites due to their greater reactivity (higher surface energy to attack in an acidic medium). This caused an increase in the average crystallite size from 28.0 to 38.9. Furthermore, for the same reason, structural defects were created that increased the density of OH groups (associated with the increased intensity of the O1s peak in the XPS results of Figure 20c), which act as redox sites or sites of transient adsorption.

Regarding the BET results in Figure 20b), the specific surface area of ZnMnAl material increased after the Cr adsorption evaluation, rising from 39.3 to 68.5 $m^2\ g^{-1}$ (Table 3) due to partial exfoliation upon loss of Zn in the acidic medium. This exfoliation, in turn, generates internal porosity, increasing accessibility to the interlayer space and facilitating the adsorption of chromium molecules.

On the other hand, in the galaxite phase, a considerable broadening and increase in intensity of the characteristic peaks were observed. This is due to a higher relative fraction of galaxite after the partial dissolution of the LDH and a structural rearrangement with greater crystallinity. This makes the phase more stable but also exposes redox defects that participate in surface Mn^{2+}/Mn^{3+} cycles, thereby contributing to electron transfer without Mn dilution (Weng et al. 2023), as shown in Figure 21 and Figure 22d) (XPS results).

Figure 20b) shows the hysteresis loops of the ZnMnAl sample before undergoing the Cr (VI) adsorption process, corresponding to type IV isotherms, exhibiting adsorption-desorption behavior typical of mesoporous materials, in which gas adsorption increases slowly as the relative saturation pressure approaches unity. In contrast, in the sample evaluated during the Cr (VI) adsorption process, gas adsorption increases without an apparent plateau, with a pronounced broadening in the relative pressure range of 0.7 to 1.0 (P/P_o). This behavior indicates a higher proportion of macropores and, consequently a larger accessible surface area, as summarized in Table 4, where for ZnAl hydrotalcite, the crystallite size increased from 28.04 nm to 38.99 nm, while for the galaxite material it increased from 12.96 nm to 13.71 nm.

Figure 20c) shows the FTIR spectra of the ZnMnAl material before and after the Cr(VI) adsorption–reducing reaction, allowing the identification of chemical changes associated with the adsorbent–adsorbate interaction.

In both spectra, a broad band in the 3300–3550 cm^{-1} region is observed, which is attributed to O–H stretching vibrations corresponding to both the structural hydroxyl groups of the ZnAl hydrotalcite and the interlayer water molecules. After Cr(VI) adsorption, this band exhibits noticeable changes mainly in shape and intensity, suggesting the involvement of –OH groups in the interaction with chromate/dichromate species through the formation of surface complexes involving –OH

consumption (Eq. 7) or through redox reactions, leading to surface dehydration or restructuring(Zhou et al. 2024) as also evidenced by the XRD results shown in Figure 20a).

Eq. 7……..$-OH + Cr + H_2O \rightarrow -CrO + H_3O^+$

The signals located around 1300–1400 cm^{-1} are associated with the vibrations of the CO_3^{2-} anion, acting as an interlayer anion, which suggests a possible partial anion exchange or a perturbation of the interlayer environment due to the incorporation of Cr(VI) species. In the 990–1080 cm^{-1} region, bands related to M–O–H vibrations and/or contributions from Cr–O bonds are observed(Deng et al. 2015); the increase in their intensity suggests the immobilization of chromium species on the surface or within the interlayer space of the material.

Likewise, the intense bands in the 570–670 cm^{-1} range are attributed to Zn–O, Al–O, and Mn–O bond vibrations(Mahjoubi et al. 2017), confirming the simultaneous presence of the hydrotalcite-like phase and Mn–Al mixed oxides (galaxite). The slight shifts and intensity changes in this region after adsorption provide evidence of a direct interaction of Cr(VI) with surface metal centers, particularly those associated with manganese.

The changes observed in the FTIR spectra after Cr(VI) adsorption suggest the formation of surface complexes mainly associated with the interaction of chromate/dichromate species with hydroxyl groups and metallic centers (especially Mn) of ZnAl–LDH/Mn–Al oxide material. This complexation mechanism, combined with anion exchange and electrostatic adsorption, accounts for the high efficiency of the material in Cr(VI) removal.

Table 3 Results of BET analysis (surface area, radius and pore volume) before and after Cr(VI) adsorption evaluation.

Sample	**S_{BET} (m^2/g)**	**Average pore Radius (Å)**	**Pore volume (cm^3/g)**
ZnMnAl	39.34	28.12	0.055
ZnMnAl-Cr	68.51	39.94	0.137

Table 4: Crystallite size values according to the phase corresponding to bi-phasic ZnMnAl material before and after the evaluation in adsorption.

Sample	***Phase***	***Crystallite size (nm)***
ZnMnAl	ZnAl-LDH	28.04
	$MnAl_2O_4$	12.96
ZnMnAl vs Cr	ZnAl-LDH	38.99
	$MnAl_2O_4$	13.71

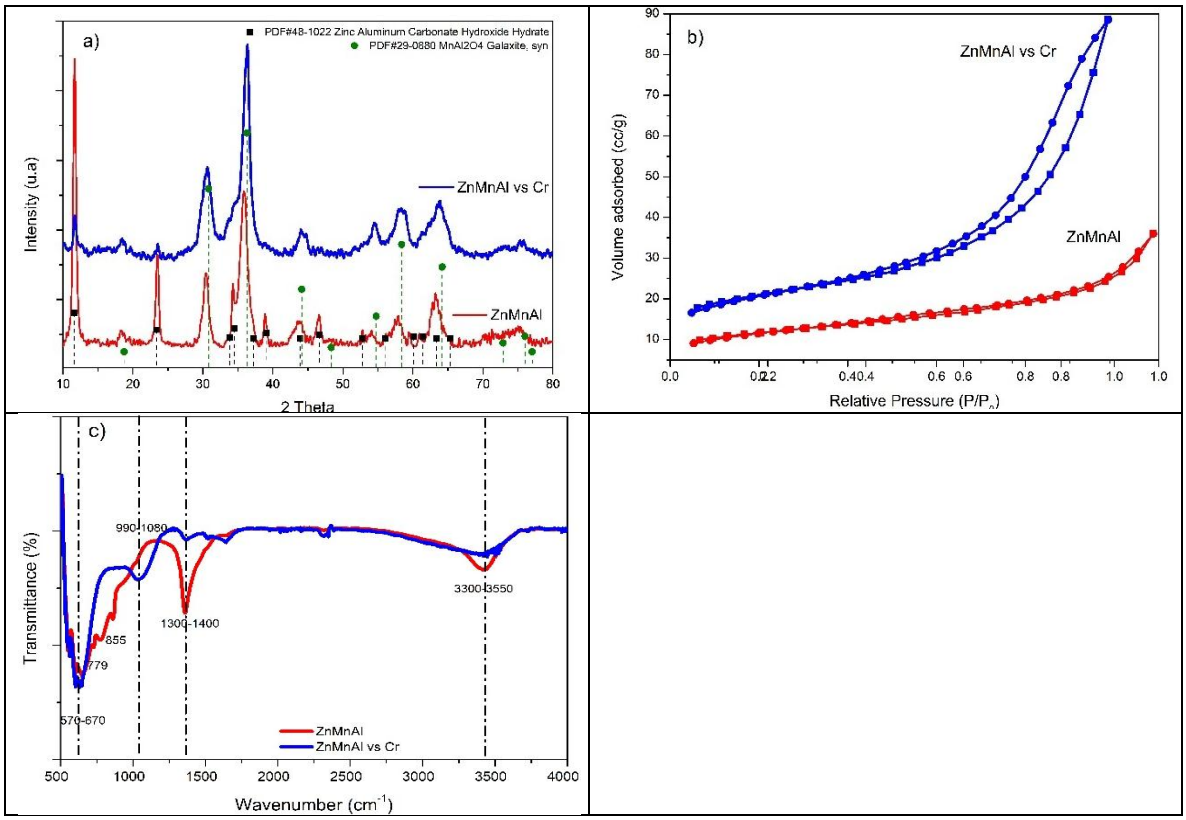
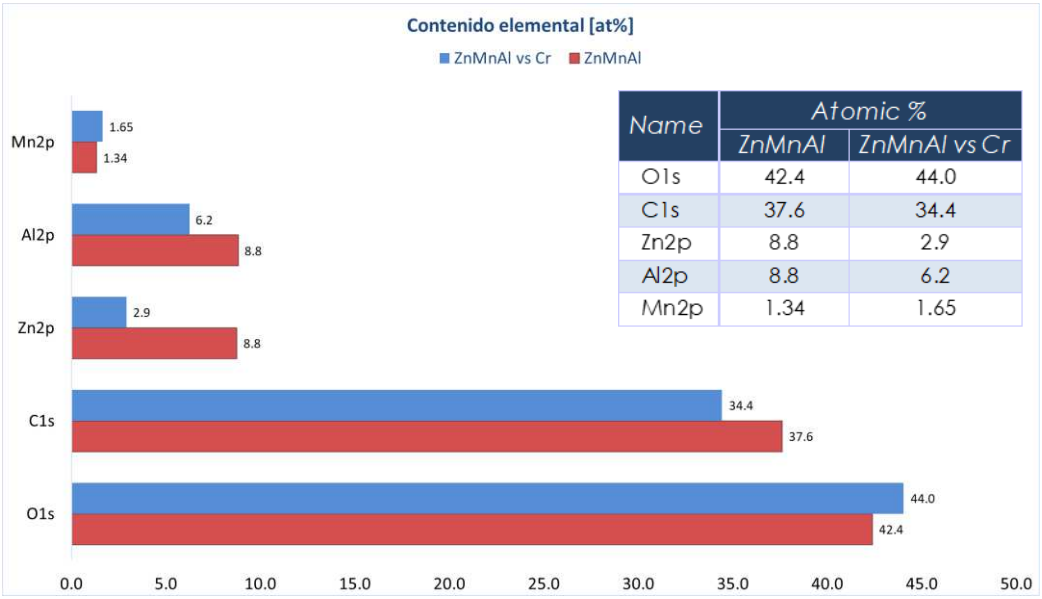


Figure 20. Comparison of a) diffractograms and b) N_2 adsorption-desorption isotherms of ZnMnAl samples before and after Cr(VI) adsorption evaluation

Figures 21 and 22 a) present the surface elemental composition of ZnMnAl material before and after the adsorption evaluation. The results reveal a decrease in the atomic percentage of Zn and Al species, along with a reduction in the O1s signal intensity, while the relative percentage of Mn species appears to increase. A more detailed discussion of each core-level signal is provided in the following paragraphs.



Name	Atomic %	
	ZnMnAl	ZnMnAl vs Cr
O1s	42.4	44.0
C1s	37.6	34.4
Zn2p	8.8	2.9
Al2p	8.8	6.2
Mn2p	1.34	1.65

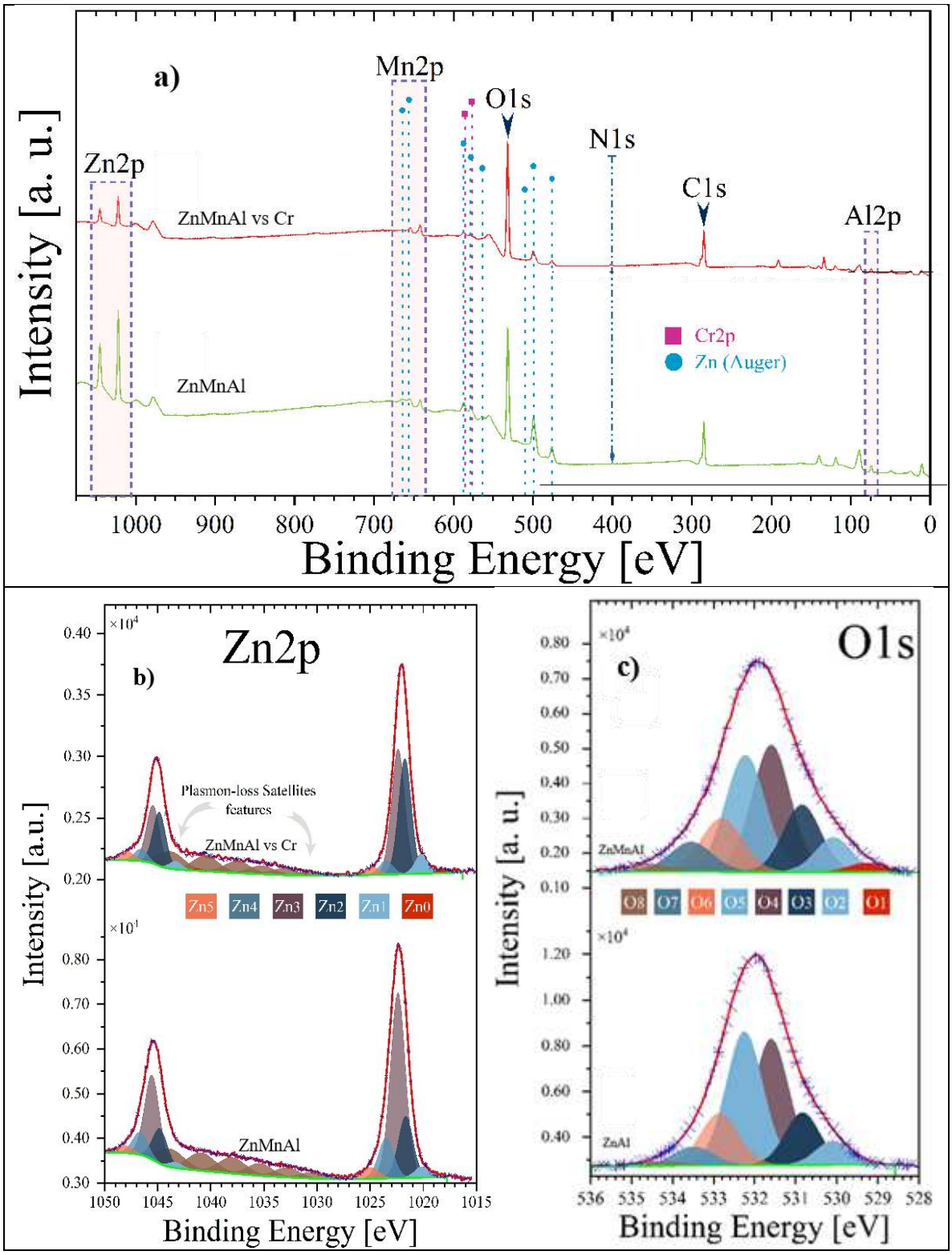
Figure 21 Atomic percentages and elemental content ratios of ZnMnAl samples

The comparative Zn2p spectra in Figure 22b) shows a slight shift of the signal toward higher binding energies after Cr(VI) adsorption. This shift is attributed to a redistribution of electron density around Zn^{2+}, induced by changes in the chemical environment of shared oxygen atoms and by inductive effects associated with the complexation of Cr–O species at neighboring sites, in agreement with the infrared spectroscopy results. Therefore, no change in the oxidation state of zinc is observed.

The shift observed in Figure 22c) corresponding to O 1s region suggests a slight increase in the amount of surface oxygen incorporated into the crystalline lattice corresponding to Mn–Al oxide phase (galaxite)(Dai et al. 2024), forming metal–oxygen bonds that replace free hydroxyl groups. This behavior is consistent with the recrystallization observed by XRD in the Figure 20a). Such recrystallization may encapsulate part of the Zn or alter its spatial distribution, as evidenced in the O 1s region.

In the Mn2p region, in Figure 22 d), the apparent decrease in intensity in the 553–556 eV range can be attributed to: spectral overlap/interference of Zn-related signals (peaks or Auger satellites) only in the measurement region, since in the overall spectrum, Cr remains constant, and its concentration even appears to increase. However, this could be because with the loss of Zinc, its concentration might increase relative to the other elements present on the surface. Therefore, the changes in this band can be ambiguously attributed to phase re-establishment, surface cover effects, or simple overlap with Zn signals during the measurement. However, the intensity of the Mn 2p spectra between approximately 640.70 eV and 642.20 eV after Cr(VI) reducing adsorption does not show significant changes, indicating that no strong interactions occurred between Cr atoms and Mn (oxides) or the ZnAl hydrotalcite, leading to incorporation into the biphasic material. Additionally, no shifts of the (003) and (006) planes toward lower angles are observed in the diffractograms(Yan et al. 2021), which would indicate an expansion of the interlayer spacing of the hydrotalcites due to Cr intercalation.

Mn oxides/mixed oxides can act as reducing agents (or reduction catalysts) for Mn^{2+}, Mn^{3+}, or other reducing species. These species may continue reducing Cr(VI) even after the removal of the solid.(Dai et al. 2024).



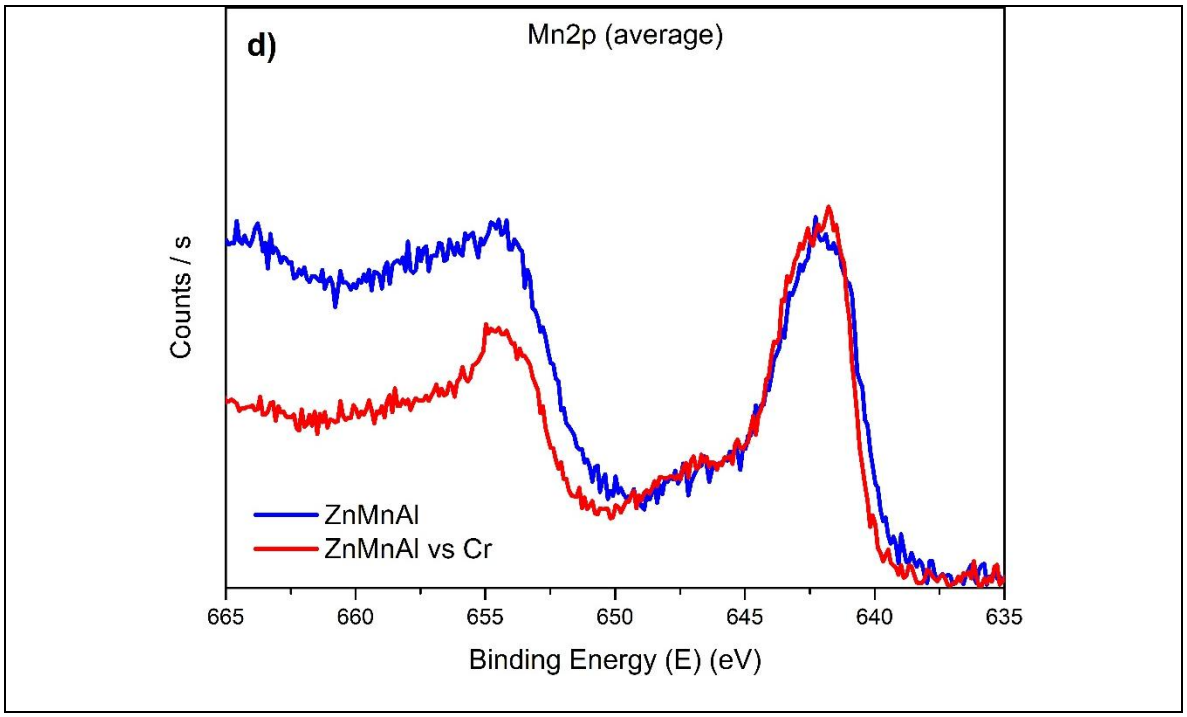


Figure 22 Comparisons of XPS results of a) general spectra b) Zn2p, c) O1s, and d) Mn2p on the ZnMnAl before and after Cr(VI) adsorption.

The ZnMnAl micrographs acquired before in the Figure 23a) and after the reducing adsorption processes in the Figure 23b) of Cr(VI) show that, prior to adsorption, the material exhibits a more compact and smooth surface. However, after evaluation, the material undergoes noticeable morphological changes, suggesting surface restructuring or partial dissolution leading to the formation of complexes(Li et al. 2025) that promote the reduction of Cr(VI) to Cr(III). This behavior is accompanied by a certain degree of surface flaking, indicating that the ZnMnAl material does not retain Cr(VI) directly.

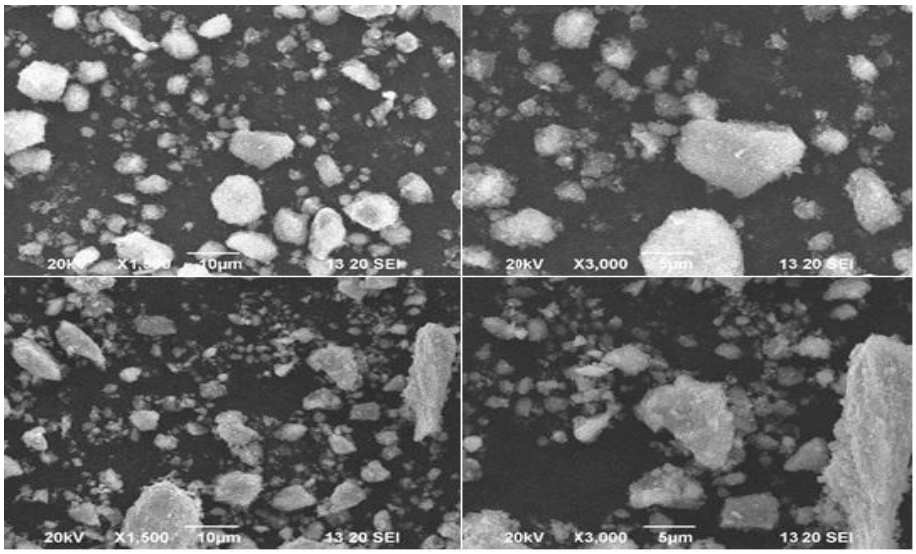


Figure 23 SEM images of a) ZnMnAl before adsorption evaluation to 1500X and 3000X and b) ZnMnAl 3after adsorption test at 1500X and 3000X.

Aqueous samples containing chromium were analyzed to determine the total (Cr) metal concentration before and after a reducing adsorption test using a two-phase material. Quantification with flame atomic absorption spectroscopy allowed for the evaluation of potential chromium removal through interaction with the material's surface.

The results indicated that the total chromium concentration in solution remained practically constant before and after the test, demonstrating that the chromium was not adsorbed onto the surface of the two-phase material. In other words, the metal remained dissolved in the solution at concentrations equivalent to the initial concentrations, indicating the absence of significant adsorption. However, a change in the solution's color was observed, shifting from the characteristic yellowish hue of chromium (VI) to a bluish-green color, as shown in Figure 24, suggesting the reduction of hexavalent chromium to trivalent chromium. Therefore, the two-phase material did not primarily act as an adsorbent but promoted a redox transformation of Cr(VI) to Cr(III), keeping the chromium in the liquid phase but in a different oxidation state.

Together with the decrease of the maximum absorption signal of Cr(VI) at 336 nm, this indicates the reduction of Cr(VI) to Cr(III) via electron transfer from the oxide phase and/or from –OH groups of the LDH. The concomitant oxidation of the material induces reorganization and recrystallization of the oxides (formation of Mn–O–Al mixed oxides), structural disorder, and intercalation within the hydrotalcite, as well as an apparent loss or attenuation of Zn and Mn surface signals (the latter likely affected by interference from Zn-related signals).

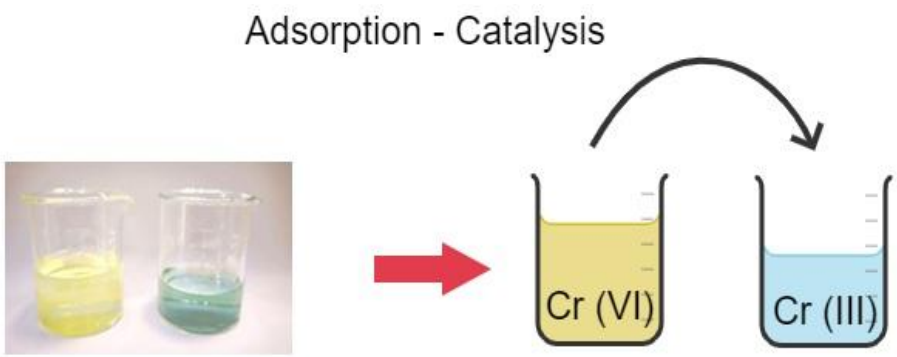


Figure 24 Color change of Cr(VI) reduced to Cr(III)

Conclusion

Incorporation of Mn into an ZnAl matrix produced a bifunctional ZnMnAl material with improved textural and chemical properties, including a higher specific surface area and slightly smaller pore size due to structural reorganization induced by Mn–Al mixed oxides. These oxides generate redox-active centers associated with Mn species, which promote coupled adsorption–reduction processes and explain the higher reducing performance and Cr(VI) removal capacity compared with ZnAl.

Adsorption experiments at pH 2 demonstrated that Cr(VI) removal occurs through a coupled adsorption–reduction mechanism. UV–Vis spectra showed the disappearance of the characteristic Cr(VI) absorption band and a color change in the solution, confirming its reduction to Cr(III).

XRD results revealed partial structural disorder in the hydrotalcite phase and reorganization of the $MnAl_2O_4$ phase after interaction with Cr(VI). However, the main crystalline phases were preserved, confirming the structural stability of the material during the process.

The highest removal efficiency at pH 2 is attributed to strong electrostatic interactions between protonated surface sites and the predominant Cr(VI) species ($HCrO_4^-$). As pH increases, the reduction in positive surface charge weakens the adsorbent–adsorbate interaction and decreases removal efficiency.

ZnMnAl material exhibited a high adsorption capacity (q_{max} = 232.56 mg g^{-1}) and strong affinity for chromium, with adsorption behavior mainly described by the Langmuir model. Overall, ZnMnAl material acts as a stable and efficient bifunctional adsorbent–catalyst with promising potential for Cr(VI) removal in aqueous systems and possible application in water treatment technologies.

References

Ahmed, M A, Mohamed, A A (2023). A systematic review of layered double hydroxide-based materials for environmental remediation of heavy metals and dye pollutants. *Inorganic Chemistry Communications*, *148*(December 2022), 110325. https://doi.org/10.1016/j.inoche.2022.110325

Cao S, Cao J, Zhu H, Huang Y, Jin, Materazzi M, (2024). Removal of HCl from gases using modified calcined Mg-Al-CO3 hydrotalcite: Performance, mechanism, and adsorption kinetics. *Fuel*, *355*(April 2023), 129445. https://doi.org/10.1016/j.fuel.2023.129445

Dai J, Wang R, Shi Z, Yang X, Zhang L (2024). Modulating the steric effect over high-index facet of MnOx catalysts to enhance toluene oxidation. *Chemical Engineering Journal*, *486*(March), 150328. https://doi.org/10.1016/j.cej.2024.150328

Deng L, Shi Z, Peng X. (2015). Adsorption of Cr(vi) onto a magnetic CoFe2O4/MgAl-LDH composite and mechanism study. *RSC Advances*, *5*(61), 49791–49801. https://doi.org/10.1039/c5ra06178d

Dey S, and Praveen Kumar V (2020). The performance of highly active manganese oxide catalysts for ambient conditions carbon monoxide oxidation. *Current Research in Green and Sustainable Chemistry*, *3*(May), 100012. https://doi.org/10.1016/j.crgsc.2020.100012

Donohue M D U, and Aranovich G L (1998). *Classification of Gibbs adsorption isotherms*. 137–152.

Feng X, Long R, Wang L, Li C, Bai Z, Liu X. (2022). A review on heavy metal ions adsorption from water by layered double hydroxide and its composites. *Separation and Purification Technology*, *284*(November 2021), 120099. https://doi.org/10.1016/j.seppur.2021.120099

Gherca D, Porcescu M, Herea D D, Chiriac H, Lupu N, Buema G (2023). Superior efficacies adsorptions on hydrotalcite-like compound as dual-functional clay nanomaterial for heavy metals and anionic dyes. *Applied Clay Science*, *233*(June 2022), 106841. https://doi.org/10.1016/j.clay.2023.106841

Gökırmak and Gülcan M (2023). Adsorption: basics, properties, and classification. *Adsorption through Advanced Nanoscale Materials: Applications in Environmental Remediation*, 3–21. https://doi.org/10.1016/B978-0-443-18456-7.00001-8

Grainca A, Boccalon E, Nocchetti M, Vivani R, Di Michele A, Longhi M, Pirola C. (2024). Sonochemical and mechanochemical synthesis of iron-based nano-hydrotalcites promoted with Cu and K as catalysts for CO and CO2 Fischer-Tropsch synthesis. *Fuel*, *373*(June), 132303. https://doi.org/10.1016/j.fuel.2024.132303

Guo Y, Zhu Z, Qiu Y, Zhao J (2012). Adsorption of arsenate on Cu/Mg/Fe/La layered double hydroxide from aqueous solutions. *Journal of Hazardous Materials*, *239–240*, 279–288. https://doi.org/10.1016/j.jhazmat.2012.08.075

Hashem M A, Moury R A, Ur Rashid M. H, Hassan A, Maoya M, Hasan Zahin M E, Miem M M, Shahadat M S (2025). Toxic chromium adsorption from tannery wastewater on thermally activated Piper betle petiole adsorbent. *Results in Surfaces and Interfaces*, *21*(June), 100632. https://doi.org/10.1016/j.rsurfi.2025.100632

He T, Li Q, Lin T, Li J, Bai S, An S, Kong X, Song Y F (2023). Recent progress on highly efficient removal of heavy metals by layered double hydroxides. *Chemical Engineering Journal*, *462*(December 2022), 142041. https://doi.org/10.1016/j.cej.2023.142041

Horsth D F, Primo J D O, Correa J S, Anaissi F J, Noirfalise X, Bittencourt C (2023). Next Sustainability Upcycling can seals into high-value boehmite-like for the synthesis of MnAl 2 O 4 : A circular economy approach. *Next Sustainability*, *2*(July), 100009. https://doi.org/10.1016/j.nxsust.2023.100009

Kecili R, and Hussain C M (2018). Mechanism of adsorption on nanomaterials. En *Nanomaterials in Chromatography: Current Trends in Chromatographic Research Technology and Techniques*. Elsevier Inc. https://doi.org/10.1016/B978-0-12-812792-6.00004-2

Khaliq A, Alyousef H A, Dahshan A, Alotaibi B M, Alrowaily A W, Alotiby M F, Ahmad K, Henaish A M A (2024). Facile sonication synthesis of MnAl2O4/ZnO nanocomposite as an advanced electrode material for supercapacitor applications. *Journal of Alloys and Compounds*, *999*(March), 174897. https://doi.org/10.1016/j.jallcom.2024.174897

Li J, Wei Y, Zou L, Luo Y, Liu Y, Li S (2025). Study on the adsorption mechanism of heavy metal ions by Thiosulfate-Intercalated ZnAl-LDH. *Inorganic Chemistry Communications*, *179*(P1), 114771. https://doi.org/10.1016/j.inoche.2025.114771

Li S, Zeng H Y, Xiong J, Xu S (2021). Polypyrrole decorated ZnTi hydrotalcite with enhanced adsorption and Cr(VI) photoreduction activity under visible-light. *Advanced Powder Technology*, *32*(8), 3090–3100. https://doi.org/10.1016/j.apt.2021.06.021

Li Y, Wang J, Li Z, Liu Q, Liu J, Liu L, Zhang X, Yu J (2013). Ultrasound assisted synthesis of Ca-Al hydrotalcite for U (VI) and Cr (VI) adsorption. *Chemical Engineering Journal*, *218*, 295–302. https://doi.org/10.1016/j.cej.2012.12.051

Madhusudan P, Lee C, Kim J O (2023). Enhanced recovery of phosphate from wastewater using hollow hierarchical hydrotalcite/hydroxide composite microspheres adsorbent. *Journal of Water Process Engineering*, *53*(April), 103897. https://doi.org/10.1016/j.jwpe.2023.103897

Mahjoubi F Z, Khalidi A, Abdennouri M, Barka N, (2017). Zn–Al layered double hydroxides intercalated with carbonate, nitrate, chloride and sulphate ions: Synthesis, characterisation and dye removal properties. *Journal of Taibah University for Science*, *11*(1), 90–100. https://doi.org/10.1016/j.jtusci.2015.10.007

Miranda A N de, Nunes W G, Maschio L J, Pereira L G F, Okamoto S, Vieira R, Doubek G (2022). Conversion of Co-Mn-Al hydrotalcites in highly active spinel-type catalysts for peroxide decomposition. *Catalysis Today*, *397–399*(April 2021), 365–374. https://doi.org/10.1016/j.cattod.2021.08.013

Nesbitt H W, Banerjee D. (1998). Interpretation of XPS Mn(2p) spectra of Mn oxyhydroxides and constraints on the mechanism of MnO2 precipitation. *American Mineralogist*, *83*(3–4), 305–315. https://doi.org/10.2138/am-1998-3-414

Nguyen T H, Tran H N, Nguyen T V, Vigneswaran S, Trinh V T, Nguyen T D, Ha Nguyen T H, Mai T N, Chao H P (2022). Single-step removal of arsenite ions from water through oxidation-coupled adsorption using Mn/Mg/Fe layered double hydroxide as catalyst and adsorbent. *Chemosphere*, *295*(February 2021), 133370.

https://doi.org/10.1016/j.chemosphere.2021.133370

Ogata F, Ueta E, Kawasaki N (2018). Characteristics of a novel adsorbent Fe–Mg-type hydrotalcite and its adsorption capability of As(III) and Cr(VI) from aqueous solution. *Journal of Industrial and Engineering Chemistry*, *59*, 56–63. https://doi.org/10.1016/j.jiec.2017.10.005

Palacio L A, Velásquez J, Echavarría A, Faro A, Ribeiro F R, Ribeiro M F (2010). Total oxidation of toluene over calcined trimetallic hydrotalcites type catalysts. *Journal of Hazardous Materials*, *177*(1–3), 407–413. https://doi.org/10.1016/j.jhazmat.2009.12.048

Picos-Benítez, Alain R, Raudel Medina-Leaños, J. R.-L., Frade, L. A. O.-, & Martínez-Vargas, B. L. (2024). Facile one-step synthesis and characterization of MnO nanoneedles and their application in solar photocatalysis. *Optical Materials*, *155*. https://doi.org/https://doi.org/10.1016/j.optmat.2024.115873

Qi, Z., Xiong, Z., Sun, X., Ma, T., Zhang, W., & Wang, G. (2024). Applied Clay Science Study on corrosion and wear resistance of Ni-Zn-Al hydrotalcite film on Aluminum alloy surface. *Applied Clay Science*, *251*(October 2023), 107323. https://doi.org/10.1016/j.clay.2024.107323

Rodríguez-gonz, V. (2021). *Layered double hydroxides and related hybrid materials for removal of pharmaceutical pollutants from water*. *288*(March). https://doi.org/10.1016/j.jenvman.2021.112399

Shen S, Li W, Guo T, Wan R, Lu X, Dai H, Li X (2025). Mechanistic insights into heavy metal adsorption on hydroxyapatite: New perspectives from dynamic adsorption behavior. *Journal of Environmental Chemical Engineering*, *13*(5), 118855. https://doi.org/10.1016/j.jece.2025.118855

Sivaranjanee R, Kumar P S, Mahalaxmi S (2022). A review on agro-based materials on the. *Chemical Engineering Research and Design*, *181*, 423–457. https://doi.org/10.1016/j.cherd.2022.04.002

Sun H, Zang X, Wang H, Li Z, Wang W, Gu A, Ye Z, Zhao S (2023). Efficient catalytic degradation of VOCs using Mn-based hydrotalcite-like compounds coupled with non-thermal plasma. *Journal of Environmental Chemical Engineering*, *11*(6), 111321. https://doi.org/10.1016/j.jece.2023.111321

Tan X. Zhang Y, Liu M, Cao J, Duan G, Cui J, Lin A (2022). Chemosphere Ultrasonic-assisted preparation of interlaced layered hydrotalcite (U – Fe / Al-LDH) for high-efficiency removal of Cr (VI): Enhancing adsorption-coupled reduction capacity and stability. *Chemosphere*, *308*(P3), 136472. https://doi.org/10.1016/j.chemosphere.2022.136472

Wang T, Li J, Wu H, Wang J, Yang Z, Wang S, Kong C. (2025). MXene-derived rod-stacked TiO2/Mn3O4 heterostructure: Oxygen vacancy and Mn–O covalency for enhanced toluene catalysis. *Journal of Alloys and Compounds*, *1041*(September), 183759. https://doi.org/10.1016/j.jallcom.2025.183759

Weng T, Chen X, Qin J, Lv Q, Shi H, Zhang L (2023). The effect of micro- and nano- γ -Al 2 O 3 on the synthetic hydrotalcite and Congo red adsorption : Site energy distribution. *Journal of Molecular Liquids*, *388*(July), 122708. https://doi.org/10.1016/j.molliq.2023.122708

Wu K, Wang M, Li A, Zhao Z, Liu T, Hao X, Yang S, Jin P (2021). The enhanced As(III) removal by Fe-Mn-Cu ternary oxide via synergistic oxidation: Performances and mechanisms. *Chemical Engineering Journal*, *406*(13), 126739. https://doi.org/10.1016/j.cej.2020.126739

Wu X, Luo B B, Chen M, Chen F (2020). Tunable surface charge of Fe, Mn substituted polyoxometalates/hydrotalcites for efficient removal of multiple dyes. *Applied Surface Science*, *509*(January). https://doi.org/10.1016/j.apsusc.2020.145344

Yan R, Feng X, Kong L, Wan Q, Zheng W, Hagio T (2021). Evenly distribution of amorphous iron sulfides on reconstructed Mg-Al hydrotalcites for improving Cr (VI) removal efficiency. *Chemical Engineering Journal*, *417*(February), 129228. https://doi.org/10.1016/j.cej.2021.129228

Yang C, Liao L, Lv G, Wu L, Mei L, Li Z (2016). Synthesis and characterization of Mn intercalated Mg-Al hydrotalcite. *Journal of Colloid and Interface Science*, *479*, 115–120. https://doi.org/10.1016/j.jcis.2016.06.057

Zhang J, Ma Y, Zhang W, Huang X, Wang X, Huang Y, Zhang P (2022). CuBi2O4/calcined ZnAlBi-LDHs heterojunction: Simultaneous removal of Cr(VI) and tetracycline through effective adsorption and photocatalytic redox. *Journal of Cleaner Production*, *365*(June), 132810. https://doi.org/10.1016/j.jclepro.2022.132810

Zhang L, Tang Y, Zhang Y, Sun W, Yang Z, Li J (2025). Novel Fe-Mn modified self-nitrogen biochar composite : Synergistic adsorption-reduction mechanisms for enhanced Cr (VI) removal in aquatic systems. *Separation and Purification Technology*, *374*(April), 133703. https://doi.org/10.1016/j.seppur.2025.133703

Zhang Y, Wang J, Chen J, Li Y, Xue Z (2022). Reconstruction and hydration of hydrotalcite response to thermal activation temperature: Enhancement of properties for magnesia castables. *Ceramics International*, *48*(21), 31245–31254. https://doi.org/10.1016/j.ceramint.2022.06.199

Zhou H, Jiang P, Kuang Y, Pu Y, Gan, Y, Yang Y (2024). Pb2+ and Cd2+ ion adsorption capability of a novel hydrotalcite-like absorbent FeMnNi-LTH in water. *Journal of Molecular Liquids*, *411*(August), 125785. https://doi.org/10.1016/j.molliq.2024.125785

Zhu T, Song X, Li T, Hu J, Qi K, Gao P, Cui R, Tang Z (2024). Simultaneous catalytic removal of complex sulfur-containing VOCs over Mn-based hydrotalcite-like compounds: Active sites and oxidation mechanism. *Separation and Purification Technology*, *339*(February), 126694. https://doi.org/10.1016/j.seppur.2024.126694

Acknowledgements

Authors thank the financial support of SECIHTI for the scholarship “Estancias Posdoctorales por México”, IPN SIP 20260250, and SA-CD-356-23.

Authors' Contributions

A. Mantilla: Validation, Supervision, Resources, Project administration, Funding acquisition, Francisco Javier Tzompantzi Morales: Resources, Investigation, Funding acquisition, L. Lartundo-Rojas: Formal analysis, Investigation, and Guadalupe Romero Ortíz: Methodology, Writing – review and editing, Writing – original draft, Visualization, Methodology, Investigation, Conceptualization.

Funding

This study received financial support from SIP 20260250 and 20260030 IPN Projects (Angeles Mantilla) and SA-CD-356-23, UAM Project (Francisco Tzompantzi).

Declarations

Ethical approval: Not applicable.

Consent to participate: Not applicable.

Consent to publish: Not applicable.

Competing interests: The authors declare no competing interests.

Data Availability Statement: The authors declare that the data supporting this study's findings are available within the paper. Should any raw data files be needed in another format, they are available from the corresponding author upon reasonable request.

Supplementary Files

This is a list of supplementary files associated with this preprint. Click to download.

- Supplementarymaterial.docx